Black hole-neutron star mergers: The first mass gap and kilonovae

P. Drozda^{1*}, K. Belczynski², R. O'Shaughnessy³, T. Bulik¹, and C.L. Fryer⁴

- Astronomical Observatory, Warsaw University, Al. Ujazdowskie 4, 00-478 Warsaw, Poland
- Nicolaus Copernicus Astronomical Center, Polish Academy of Sciences, ul. Bartycka 18, 00-716 Warsaw, Poland
- Center for Computational Relativity and Gravitation, Rochester Institute of Technology, Rochester, NY 14623, USA
- CCS-2, MSD409, Los Alamos National Laboratory, Los Alamos, NM 87545, USA

January 2, 2023

ABSTRACT

Observations of X-ray binaries indicate a dearth of compact objects in the mass range from $\sim 2-5 \, \mathrm{M}_{\odot}$. The existence of this (first mass) gap has been used to discriminate between proposed engines behind core-collapse supernovae. From LIGO/Virgo observations of binary compact remnant masses, several candidate first mass gap objects (either neutron stars (NSs) or black holes (BHs)) were identified during the O3 science run. Motivated by these new observations, we study the formation of BH-NS mergers in the framework of isolated classical binary evolution, using population synthesis methods to evolve large populations of binary stars (Population I and II) across cosmic time. We present results on the NS to BH mass ratios ($q = M_{NS}/M_{BH}$) in merging systems, showing that although systems with a mass ratio as low as q = 0.02 can exist, typically BH-NS systems form with moderate mass ratios q = 0.1 - 0.2. If we adopt a delayed supernova engine, we conclude that ~ 30% of BH-NS mergers may host at least one compact object in the first mass gap (FMG°). Even allowing for uncertainties in the processes behind compact object formation, we expect the fraction of BH-NS systems ejecting mass during the merger to be small (from $\sim 0.6 - 9\%$). In our reference model, we assume: (i) the formation of compact objects within the FMG, (ii) natal NS/BH kicks decreased by fallback, (iii) low BH spins due to Tayler-Spruit angular momentum transport in massive stars. We find that ≤ 1% of BH-NS mergers will have any mass ejection and about the same percentage will produce kilonova bright enough to have a chance of being detected with a large (Subaru-class) 8m telescope. Interestingly, all these mergers will have both a BH and an NS in the FMG.

Key words. Stars: massive, stars: neutron, black hole physics, gravitational waves

Observations of X-ray binaries indicate a dearth of compact object mass) gap has been used to discriminate between proposed engines of binary compact remnant masses, several candidate first mass gidentified during the O3 science run. Motivated by these new observed isolated classical binary evolution, using population synthesis m II) across cosmic time. We present results on the NS to BH mass r systems with a mass ratio as low as q = 0.02 can exist, typically If we adopt a delayed supernova engine, we conclude that ~ 309 first mass gap (FMG°). Even allowing for uncertainties in the pr of BH-NS systems ejecting mass during the merger to be small formation of compact objects within the FMG, (ii) natal NS/BH k angular momentum transport in massive stars. We find that \leq 1 same percentage will produce kilonova bright enough to have a continuous distribution of compact remnants, neutron stars (NSs) and black (BHs), in a mass range from ~ 2 - 5 M_☉ (Bailyn et al. (1998),Özel et al. (2010)). These observations contradicted the prevailing theory at the time that argued for a continuous distribution of compact remnants across this range (Fryer & Kalogera 2001). One explanation for this mass gap is that the current systems were the result of an observational bias (Farr et al. 2011; Kreidberg et al. 2012). Certainly, there has been a set of observed systems with measurements within the mass gap region, for example: the recent observation of an NS with a mass of 2.14+0.09 M_☉ (Cromartie et al. 2019), the low-mass X-ray binary with a black hole mass of 3.3-0.7 M_☉ (Thompson et al. (2019)), and the ambiguous smaller component in the merger event GW190814 with mass $m_2 = 2.59+0.08 \atop 0.09 \atop$ properties of the core-collapse supernova engine (Belczynski et al. 2012). Alternatively, compact objects in the mass gap could be created by mergers of lighter compact objects, and thus probe globular cluster dynamics. This would allow such compact objects to acquire companions, which leads to second generation merges (Fragione & Loeb 2019; Fragione et al. 2020).

So far, no BH-NS binaries have been detected through electromagnetic (EM) observations (Liu et al. 2014; Bhattacharya et al. 2019). Although observations of X-ray binaries suggest that such systems should exist, the formation rate of merging BH-NS binaries is not well constrained through EM observations (Belczynski et al. 2011, 2012, 2013; Beldycki & Belczynski 2016).

The LIGO/Virgo gravitational wave detectors are ideally suited to studying the properties of compact remnants and answering questions about the existence of a mass gap. The primary gravitational wave (GW) signals for this ground-based detector consortium arise from the merger of double compact objects: BH-BH, BH-NS, and NS-NS. The first two LIGO/Virgo science runs (O1 and O2) detected 11 merging compact binaries: 10 BH-BH and 1 NS-NS (Abbott et al. 2019). Although these observations brought a wealth of information about BHs and NSs, no BH-NS mergers were observed and no compact object was reported to have mass in the mass gap region (Abbott et al. 2019a).

This picture is changing as data from the third (O3) LIGO/Virgo science run are published. Table 1 shows the most confident candidates associated with the mass gap from the O3 science run. Four events were classified as BH-NS mergers (Abbott et al. 2021; The LIGO Scientific Collaboration et al. 2021), and one as either a BH-BH or a BH-NS merger because the lighter compact object lies in the first mass gap (FMG) and its nature is currently unknown (Abbott et al. 2020).

We note that LIGO/Virgo's prompt classification scheme adopts specific choices about how to characterize compact objects that differ from those typically assumed in the literature: NSs are objects with mass $M < 3 M_{\odot}$, FMG objects have mass $3 < M < 5 \,\mathrm{M}_{\odot}$, and BHs have mass $M > 5 \,\mathrm{M}_{\odot}$. This clas-

^{*} paweldro1996@gmail.com

sification means that any type of actual double compact object (NS-NS, BH-NS, or BH-BH) can have one or two FMG objects as long as the true mass limit discriminating between NSs and BHs is anywhere between $\sim 2-5~M_{\odot}$.

GW (gravitational wave) ground based observations can identify the FMG objects, but they cannot easily distinguish between low-mass BHs or high-mass NSs (e.g., Hinderer et al. (2019)). EM observations can possibly help to identify the nature of a given FMG object. For example, the expectation is that BH-BH mergers do not produce EM emission, and no EM counterpart has been found so far for such a merger (e.g., Greiner et al. (2016)). For BH-NS and NS-NS mergers, various EM counterparts are expected across the EM spectrum. The most notable are short gamma-ray bursts (Paczyński 1991; Lee & Kluzniak 1995; Ruffert et al. 1997) and kilonovae (Li & Paczyński 1998). Although there are expected differences between the composition of the ejecta, depending on the size and nature (NS vs. BH) of the compact remnant, the differences are currently difficult to disentangle from the many model uncertainties (e.g., Metzger (2017); Miller et al. (2019a); Korobkin et al. (2020)). However, by better understanding BH-NS properties, there is hope to better differentiate between BH-NS and NS-NS systems.

In this study we focus on BH-NS mergers that form in classical (common envelope (CE)) isolated binary evolution (e.g., Belczynski et al. (2016)). We estimate the typical physical properties of these mergers that LIGO/Virgo could detect. Using population synthesis models that include updated estimates of BH spins and masses (Belczynski et al. 2020), we estimate the fraction of BH-NS mergers that host FMG objects. We also estimate the amount of mass ejection during BH-NS mergers, estimating the nature and detectability of any associated kilonova emission.

2. Calculations

2.1. Evolutionary calculations

In this paper, we evolve populations of massive star binaries in order to estimate the population of BH-NS binaries, focusing on those systems that merge in the Hubble time. All models we present were obtained using the StarTrack population synthesis code (Belczynski et al. 2002, 2008a; Belczynski et al. 2020) under the isolated classical (CE) binary evolution scenario. We calculate a series of models with different prescriptions for stellar evolution and binary input physics. For each model, we use a range of metallicity Z from 0.0001 up to 0.03: 32 sub-models with the same input physics but with different metallicity, each calculated for 2×10^7 massive binaries. In this section, we re-

Table 1. LIGO/Virgo BH-NS merger candidates

ID	$m_1/~M_{\odot}$	$m_2/~M_{\odot}$	q	type
GW190426	$5.7^{+3.9}_{-2.3}$	$1.5^{+0.8}_{-0.5}$	$0.27^{+0.42}_{-0.17}$	BH-NS
GW190814	$23.2^{+1.1}_{-1.0}$	$2.59^{+0.08}_{-0.09}$	$0.112^{+0.008}_{-0.009}$	BH-FMG ^a
GW190917	$9.3^{+3.4}_{-4.4}$	$2.1_{-0.5}^{+1.5}$	$0.2^{+0.34}_{-0.09}$	BH-NS
GW200105	$8.9^{+1.1}_{-1.3}$	$1.9^{+0.2}_{-0.2}$	$0.21^{+0.06}_{-0.04}$	BH-NS
GW200115	$5.9^{+1.4}_{-2.1}$	$1.4^{+0.6}_{-0.2}$	$0.24^{+0.31}_{-0.08}$	BH-NS

^a: This merger consisted of a BH and the first mass gap object (FMG), the nature of which is unknown (either an NS or a BH).

view the assumed initial conditions and the basic prescriptions used for binary evolution.

We used initial binary parameters from Sana et al. (2012) as modified by de Mink & Belczynski (2015), and stellar winds were adopted from Vink et al. (2001) and Belczynski et al. (2010). We used a 50% binary fraction and we assumed a maximum NS mass of 2.5 M_{\odot} . We adopted a solar metallicity of $Z_{\odot}=0.014$.

We adopt three component broken power-law initial mass functions (IMFs) from Kroupa (2001) for the primary (more massive) component in each binary: $M_{ZAMS,A} \propto M^{-1.3}$ for $0.08 \leq M < 0.5 \, \mathrm{M_\odot}$, $\propto M^{-2.2}$ for $0.5 \leq M < 1.0 \, \mathrm{M_\odot}$, and $\propto M^{-\alpha_3}$ for $1.0 \leq M < 150 \, \mathrm{M_\odot}$, where we adopt $\alpha_3 = 2.3$. The initial mass of the secondary $(M_{ZAMS,B})$ binary component is taken from the flat mass ratio distribution in a range $q_0 = [0.08/M_{ZAMS,A}, 1]$, where $q_0 = M_{ZAMS,B}/M_{ZAMS,A}$. The lower range limit is chosen in such a way in order to provide second component mass above the hydrogen burning limit $(0.08 \, \mathrm{M_\odot})$.

In our CE calculations, we use an energy balance approach from Webbink (1984), with updates on binding envelope energy from Dominik et al. (2012). We do not take into account systems in which a CE with a Hertzsprung gap donor occurred, as we conservatively assume these merge during the CE phase. The core-envelope structure of these stars is not well known (Belczynski et al. 2007; Ivanova et al. 2013) and the survival of these systems during CE is highly uncertain. Additionally, such systems may evolve through thermal timescale Rochelobe overflow (RLOF) rather than through CE (Pavlovskii et al. 2017). We adopted an accretion rate of 5% of the Bondi-Hoyle rate (MacLeod et al. 2017) onto the NS and BH during the CE phase.

During stable RLOF with an NS and BH accretor, we calculate binary evolution and component masses using prescriptions from Mondal et al. (2020). In all the other cases, we assume a nonconservative mass transfer, with 50% of the transferred mass being lost from a binary with high specific angular momentum $j_{\rm loss}=1$ (Podsiadlowski et al. 1992). The remaining 50% of the transferred mass is attached to a companion star.

Following Fryer et al. (2012), we use a neutrino supported convective supernova engine to deduce the masses of NSs and BHs in our simulations. We allow for a different development time of such an engine. In the rapid supernova model, for intermediate-mass stars, the engine develops very quickly ($\sim 100~\text{ms}$) and is followed by a supernova explosion and the ejection of stellar outer layers , and light NSs form. For massive stars, the engine is not able to overcome the weight of in-falling outer stellar layers and stars collapse to form rather massive BHs. This naturally creates a mass gap between NSs and BHs (Belczynski et al. 2012). In the delayed supernova model, the engine develops after a relatively long time ($\sim 500-1000~\text{ms}$) after core collapse. This allows for significant accretion ($\sim 1-2~\text{M}_\odot$) onto light proto-NSs, and the formation of heavy NSs and light BHs producing a continuous mass spectrum of compact objects.

The FMG is typically defined as the range: $\sim 2-5~M_{\odot}.$ To reflect the recently discovered (in radio) NSs with masses of about 2.1 M_{\odot} (see Cromartie et al. (2019), Zhang & Li (2019)), we adopt a slightly narrower range as a definition of the FMG: $2.1-5~M_{\odot}$ in our calculations.

For massive stars, we take into account pair-instability pulsation supernova mass loss. We adopt the weak mass loss that allows for the formation of BHs up to $\sim 55~M_{\odot}$ (Belczynski et al. 2020). We also allow for the most massive stars to be totally disrupted (no BH remnant) by pair-instability supernovae. During

NS and BH formation, we assume 10% and 1% neutrino mass loss, respectively.

Compact objects during formation may receive natal kicks (Hobbs et al. 2005). We use a one dimensional Maxwellian natal kick magnitude distribution with $\sigma=265~\rm km~s^{-1}$. This generates a three dimensional average speed of $\sim420~\rm km~s^{-1}$. The orientation of the natal kick is random. For some models, we allow kicks to be decreased in magnitude through fallback of matter during compact object formation. The natal kick decreases with decreasing ejecta mass (increasing fallback mass):

$$V_{kick} = (1 - f_{fb})V, \tag{1}$$

where V is the kick magnitude drawn from the Maxwellian distribution with $\sigma=265~{\rm km~s^{-1}}$, and f_{fb} is a fraction of matter that falls back onto a compact object after the supernova explosion. The fallback fraction f_b is obtained from formulae by Fryer et al. (2012). It should be noted that this fallback of matter during core collapse is always used in the calculation of compact object mass, but is used only for some models in the calculation of natal kicks. In other words, when fallback is applied, we assume asymmetric mass ejection natal kicks, and when fallback is not applied, we assume asymmetric neutrino emission driven natal kicks. For a more detailed discussion about natal kicks, see Section 6 of Belczynski et al. (2016).

The natal BH spin magnitude $(a_{\text{spin}} = (cJ)/(GM^2)$, where J and M are BH angular momentum and mass, respectively) is estimated using one of three different prescriptions of angular momentum transport in stellar interiors, depending on the simulation performed. The most efficient angular momentum transport is adopted from Fuller & Ma (2019); Fuller et al. (2019) and we assign $a_{\rm spin} = 0.01$ for each BH natal spin in this scenario. The next scenario employs the standard Tayler-Spruit magnetic dynamo and efficient angular momentum transport from Spruit (1999) as adopted in the MESA evolutionary code; this model results in $a_{\rm spin} \approx 0.05 - 0.15$ depending on progenitor star mass and metallicity. Finally, we also adopt an inefficient angular momentum transport driven by meridional currents (Ekström et al. 2012) as used in the Geneva evolutionary code; this results in $a_{\rm spin} \approx 0.9$ for low-mass BHs ($\lesssim 20 {\rm M}_{\odot}$) and $a_{\rm spin} \approx 0.2$ for high-mass BHs ($\gtrsim 20 \, M_{\odot}$). Full details of the three models are given in Belczynski et al. (2020).

The natal BH spin magnitude may be affected by tidal interactions between the stars in progenitor binaries of BH-NS mergers. Therefore, we allow for tidal spin-up. If a Wolf-Rayet (WR) star forms in a sufficiently close binary, it is subject to strong tidal interactions, which affect its rotation in comparison to single stellar evolution models (see Hotokezaka & Piran (2017), Qin et al. (2018)). The resultant spin of a BH formed from such a star will be different from the spin of a BH that was formed either in isolation or in a wide binary. We adopt natal BH spin magnitudes formed from tidally affected WR stars from Belczynski et al. (2020):

$$a_{\rm spin} = e^{-0.1(P_{\rm orb}/P_0 - 1)^{1.1}} + 0.125,$$
 (2)

where $P_{\rm orb}[s]$ is the orbital period and $P_0 = 4000s$. We apply this formula for $P_{\rm orb} = 0.1 - 1.3$ days. We assume that wider systems (with $P_{orb} > 1.3$ days) do not experience significant tidal interactions. BHs originating from binaries with $P_{orb} < 0.1$ days are assigned a spin magnitude of $a_{\rm spin} = 1.0$.

Table 2 contains list of our models.

Table 2. Calculated models, Supernova engine: R/D - rapid/delayed.

Model	Supernova engine	fallback	BH spin
M230	R	1	MESA
M233	R	0	MESA
M280	D	1	MESA
M283	D	0	MESA
M383	D	0	Geneva
M483	D	0	Fuller

2.2. BH-NS merger mass ejection and kilonovae

When an NS is disrupted in a BH-NS merger, the radioactive ejecta can emit a burst of electromagnetic radiation known as a kilonova. We do not consider other potential electromagnetic signals in this study (e.g., jets producing short gamma-ray bursts considered by Postnov et al. (2019)).

During the merger there are two basic scenarios: (i) the NS is disrupted outside the BH event horizon (potential EM signal), or (ii) the NS is disrupted inside the BH event horizon (no EM signal). What happens depends on the BH spin, the NS equation of state (EoS), the mass ratio of two compact objects and the orientation of the NS orbit with respect to the BH spin plane. For each BH-NS binary system that we form in our population synthesis calculations, we consider all these parameters. We determine the ejecta mass from Kawaguchi et al. (2016):

$$\begin{split} \frac{M_{ej}}{M_{NS,b}} &= \max\{a_1 Q^{n_1} (1 - 2C_{NS}) C_{NS}^{-1} \\ &- a_2 Q^{n_2} \tilde{r}_{ISCO} \left(a_{\text{spin}} \cdot cos(i_{\text{tilt}}) \right) + a_3 \left(1 - \frac{M_{NS}}{M_{NS,b}} \right) + a_4, 0\}, \quad (3) \end{split}$$

where $Q = M_{BH}/M_{NS}$ (M_{BH} is BH mass and M_{NS} is NS mass), $i_{\rm tilt}$ is the angle between BH spin and orbital angular momentum, and $C_{NS} = GM_{NS}/(c^2R_{NS})$ is the NS compactness parameter that depends on the EoS. M_{NS} and R_{NS} are neutron star mass and radius, respectively.

We use the *MPA1* NS *EoS*, which is consistent with observational constraints on neutron star tidal deformation from the first NS-NS merger observation (see Fig. 1), as well as neutron star interior composition explorer (NICER) observations (Miller et al. 2019b). We employ (and this figure shows) mass-radius estimates for several *EoS s* drawn from 1 . The maximum NS mass for the MPA1 equation of state is $\sim 2.46~M_{\odot}$. Rather than treat objects with masses between $2.46M_{\odot}$ and $2.5M_{\odot}$ as black holes ($\lesssim 1\%$ of NSs in BH-NS mergers in our models), we assume a constant mass-radius relation for objects in this mass range and we treat them as neutron stars. A 2.46 M_{\odot} NS has 11.3 km radius, and then all NSs above this mass (up to 2.5 M_{\odot}) have 11.3 km radius.

The parameters a_1 - a_4 , n_1 , and n_2 are discussed in Kawaguchi et al. (2016). $M_{NS,b}$ is the total baryonic mass of an NS. We use the relation between M_{NS} and $M_{NS,b}$ for nonrotating NS from Gao et al. (2020) and Gupta et al. (2019), lowered by 1.8% to account for the relative error of NS baryonic mass estimation (a lower $M_{NS,b}$ provides more realistic ejecta masses). \tilde{r}_{ISCO} is the innermost stable circular orbit radius normalized by M_{BH} (e.g., from Foucart et al. (2018)):

$$\tilde{r}_{ISCO} = \frac{r_{ISCO}}{GM_{BH}c^{-2}} = 3 + Z_2 - \text{sign}(a_{\text{spin}}) \sqrt{(3 - Z_1)(3 + Z_1 + 2Z_2)},$$

¹ https://www3.mpifr-bonn.mpg.de/staff/pfreire/ interests.html

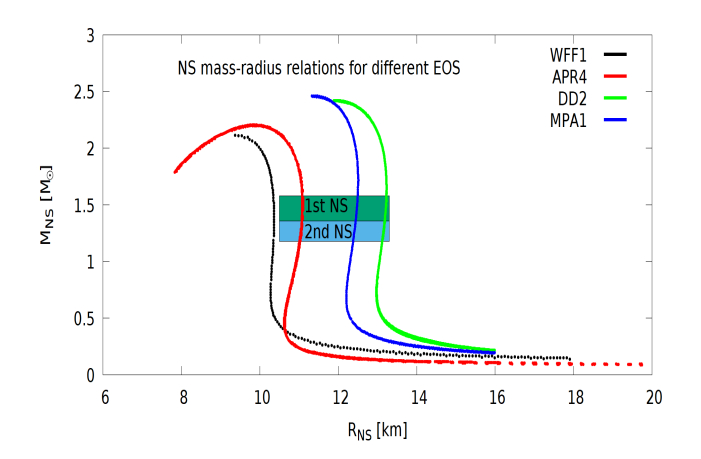


Fig. 1. Comparison of the NS mass-radius relation of four different equations of state (EoSs) with the LIGO/Virgo constraints from NS-NS merger GW170817 (90% credible limits shown by green and blue boxes: Abbott et al. (2018a)). We employ the MPA1 EoS, which reaches ~ 2.5 M_☉ (our adopted maximum NS mass) and agrees with the LIGO/Virgo constraints. Other relations are WFF1 (Wiringa et al. 1988), APR4 (Akmal et al. 1998), and DD2 (Alvarez-Castillo et al. 2016).

(4)

where Z_1 and Z_2 are functions of BH spin, and $Z_1 = 1 + (1 - a_{\rm spin}^2)^{1/3}((1 + a_{\rm spin})^{1/3} + (1 + a_{\rm spin})^{1/3})$ and $Z_2 = \sqrt{3a_{\rm spin}^2 + Z_1^2}$. However, we use the projection of BH spin on the binary orbital momentum direction to calculate \tilde{r}_{ISCO} ($\tilde{r}_{ISCO}(a_{\rm spin} \cdot \cos(i_{\rm tilt}))$).

Kilonova emission remains an active area of research and the peak luminosity depends on a wide range of factors concerning the properties of the ejecta, such as their composition, their morphology, and the viewing angle (see Wollaeger et al. (2019), Wollaeger et al. (2018), Zhu et al. (2018), Fontes et al. (2020), and Korobkin et al. (2020)). For this paper, we use the following parameterized formula for the o-band (1260–1360 nm) peak luminosity:

$$L_{peak} = f \times 10^{40} \left(\frac{M_{ej}}{0.01 \text{ M}_{\odot}} \right)^{0.2} \left(\frac{v}{0.1c} \right)^{0.2} \text{erg s}^{-1},$$
 (5)

where f is varied to match the wide range of current results: $0.3 \le f \le 4.5$. We assume that f has uniform distribution in this range. For ejecta velocity, we use the formula from Kawaguchi et al. (2016):

$$v/c = 0.01533Q + 0.1907.$$
 (6)

We calculate apparent flux from the kilonova for each merger event with mass ejection. We assume that mass ejection is isotropic. Therefore, the flux can be calculated as:

$$F = \frac{L_{peak}/(1+z)^2}{4\pi D_I^2},$$
(7)

where z is redshift and D_L is the luminosity distance of a given merger.

This flux corresponds to the apparent o-band magnitude on Earth. The apparent kilonova magnitude can be calculated using Pogson's equation:

$$M_{kn} = m_{\text{Vega}} - 2.5 \log_{10} \left(\frac{F}{F_{Vega}} \right),$$
 (8)

Article number, page 4 of 15

where $m_{\text{Vega}} = 0.026$ mag is the apparent Vega magnitude as seen from Earth, $F_{Vega} = 2.18072 \times 10^{-8} \text{ W m}^{-2}$ is flux from Vega, and F is flux from the kilonova.

2.3. Cosmology

We assume a flat Universe with $\Omega_M = 0.3$, $\Omega_{\Lambda} = 0.7$, $\Omega_k = 0$ (Ade et al. (2016)), and Hubble constant $H_0 = 68.7 \text{ km s}^{-1} \text{ Mpc}^{-1}$. This gives the age of Universe $t_0 \sim 13.7 \text{Gyr}$ (Aghanim et al. 2018; Hinshaw et al. 2013).

We assume that binary stars (Population I and II) are formed in the redshift range z = 0 - 15. The star formation rate density history is adopted from Madau & Fragos (2017):

sfrd(z) =
$$0.015 \frac{(z+1)^{2.6}}{1 + ((z+1)/3.2)^{6.2}} \text{ M}_{\odot} \text{ Mpc}^{-3} \text{ yr}^{-1}$$
. (9)

We adopt an average cosmic metallicity evolution from Madau & Fragos (2017) and we adopt a Gaussian distribution (with 0.5 dex sigma) of metallicity around the average at each redshift (Belczynski et al. 2020). After evolution, some binaries form BH-NS systems and some of these systems merge. We record their merger redshifts (and corresponding distances). We also calculate an intrinsic BH-NS merger rate density and an intrinsic merger rate as a function of redshift for all of our models, following the method described in detail by Belczynski et al. (2016).

2.4. Result presentation

The results of our simulations are presented in the context of intrinsic properties of binary systems, as well as the properties of the subset of systems likely to be detected by LIGO/Virgo. We mostly focus on low redshift systems (z < 1) because BH-NS mergers will not be detected by LIGO/Virgo above redshift z = 1 even at full design sensitivity. We also present results based on the current sensitivity limits of the LIGO/Virgo O3 science run.

We present the intrinsic fraction of BH-NS mergers that have compact object or objects in the FMG, which we estimate from:

$$\eta_1 = \frac{Rd_{fmg,z<1}}{Rd_{z<1}},\tag{10}$$

where $Rd_{fmg,z<1}$ (Gpc^{-3} yr^{-1}) is the intrinsic merger rate density for BH-NS mergers that occur for redshifts z<1 and that have two, one, or no objects within the FMG (assumed $2.1-5~M_{\odot}$ range, see Sec. 2.1). If there is only one compact object within the FMG, we identify whether it is an NS or a BH (using our $2.5~M_{\odot}$ maximum mass limit for an NS). $Rd_{z<1}$ (Gpc^{-3} yr^{-1}) is the intrinsic merger rate density for all z<1 BH-NS mergers.

To present results for mass ejection in mergers of BH-NS binaries, we use a fraction of intrinsic merger rate density. The intrinsic fraction of z < 1 BH-NS mergers with some mass ejection is found from:

$$\eta_2 = \frac{Rd_{Mej,z<1}}{Rd_{z<1}},\tag{11}$$

where $Rd_{Mej,z<1}$ (Gpc^{-3} yr^{-1}) is the intrinsic merger rate density for BH-NS mergers that occur at redshifts z<1 and has an ejecta mass $M_{ej}>0.001~{\rm M}_{\odot}$ or $M_{ej}>0.01~{\rm M}_{\odot}$, and $Rd_{z<1}$ (Gpc^{-3} yr^{-1}) is the intrinsic merger rate density for all z<1 BH-NS mergers.

Using simple mass scaling, we assess the detectability of BH-NS mergers in gravitational waves by LIGO/Virgo. We assume that BH-NS mergers are only detectable if the signal-to-noise ratio (S/R) in one LIGO/Virgo detector is larger than 8, and we estimate a fiducial S/R from:

$$S/R = 8.0 \frac{120 \text{Mpc}}{D_L} \left(\frac{M_{chirp}}{1.2 \text{ M}_{\odot}} \right)^{5/6}, \tag{12}$$

where $M_{chirp} = (m_1 m_2)^{3/5} (m_1 + m_2)^{-1/5}$ is the chirp mass of the BH-NS system, and m_1 and m_2 are BH-NS components masses. In this formula, we assume that the current O3 LIGO/Virgo detection range for an NS-NS merger with a typical chirp mass of 1.2 $\rm M_{\odot}$ is 120 Mpc (Abbott et al. 2018b)), and we average over the source orientation and sky location. This gives us a detection rate of BH-NS mergers by LIGO/Virgo: R_{ligo} yr⁻¹. The fraction of BH-NS mergers that have compact objects in the FMG that are detectable by LIGO/Virgo is calculated from:

$$\eta_3 = \frac{R_{fmg,ligo}}{R_{ligo}},\tag{13}$$

where $R_{fmg,ligo}$ (yr⁻¹) is the LIGO/Virgo detection rate of BH-NS mergers that have two, one or no objects within the FMG.

We also calculate the fraction of LIGO/Virgo detectable BH-NS mergers (S/R > 8) that show some mass ejection ($M_{\rm ej}$) during the merger process as:

$$\eta_4 = \frac{R_{Mej,ligo}}{R_{ligo}},\tag{14}$$

where R_{ligo} (yr⁻¹) is the LIGO/Virgo detection rate of BH-NS mergers, and $R_{Mej,ligo}$ (yr⁻¹) is the detection rate of BH-NS mergers with M_{ei} larger than a specified value (i.e., $M_{ei} > 0.001$ M_{\odot}).

BH-NS mergers that are detectable as kilonovae are defined as follows: first, they need to be detectable by LIGO/Virgo (S/R > 8) and then they need to have enough mass ejecta escaping with appropriate speed during the merger to produce emission bright enough to be detected by a given telescope (see eq. 5). For each BH-NS merger with mass ejection (and kilonova), we use its apparent magnitude $(M_{\rm kn}$, see eq. 8) and compare it with the threshold sensitivity of three different telescopes that are employed in the search for kilonovae.

We consider a range of telescopes, from small instruments that can cover a large fraction of the sky, such as ATLAS (2 telescopes, each with a diameter of 0.5m) with a maximum reach of $M_{\rm max}=19.5$ mag (exposure time 0.5min), to the medium-size Canada-France-Hawaii Telescope (CFHT) (1 telescope with a diameter of 3.6m) with 24.1mag limit (exposure time 60min), and the large Subaru telescope (1 telescope with a diameter of 8.2m) with a limit of 26.0mag (exposure time 4 – 8min). These exposure times are adopted from the official cameras' specifications as characteristic times at certain bands.

ATLAS's detection limit is given directly for o-band, while the CFHT and Subaru limits are adopted for J-band (WIRCam camera limit, band centered at 1220 nm) and Ic filter (Suprime – Cam camera limit (see Miyazaki et al. (2002)), filter centered at 806 nm), respectively. If a kilonova is brighter than the threshold for a given telescope:

$$M_{\rm kn} < M_{\rm max} \tag{15}$$

then we call it a detectable EM/kilonova counterpart to a given LIGO/Virgo BH-NS merger signal. Then we calculate the fraction of detectable BH-NS mergers as kilonova that are brighter

than chosen telescope brightness threshold (see eq. 15) in all LIGO/Virgo detectable BH-NS mergers from:

$$\eta_5 = \frac{R_{kn,ligo}}{R_{ligo}},\tag{16}$$

where $R_{kn,ligo}$ (yr⁻¹) is the LIGO/Virgo detection rate of BH-NS mergers with detectable kilonovas, and R_{ligo} (yr⁻¹) is the LIGO/Virgo detection rate of BH-NS mergers.

It should be noted that the above scheme does not account for any localization issues that may arise during the search for kilonovae associated with LIGO/Virgo sources (e.g., Nissanke et al. (2013); Gomez et al. (2019)). This approximation serves only as a guide to inform us whether any given kilonova is bright enough to be detected (with some typical exposure time) by a given telescope, if this telescope was pointed right at the kilonova. Additionally, we use peak brightness, so this is a very optimistic approximation of kilonova detectability.

3. First mass gap objects in BH-NS mergers

First we study the BH-NS merger compact object mass distribution (z < 1) for several evolutionary models (M230, M233, M280, and M283) using both rapid (Figure 2) and delayed (Figure 3) supernova engine prescriptions for remnant masses. As expected, the FMG is clearly visible in models that employ a rapid supernova engine (e.g., M230 and M233). Therefore, for these models, we do not expect BH-NS mergers with compact objects of comparable mass. However, for models that employ a delayed supernova engine (e.g., M280 and M283), there is no mass gap between NSs and BHs, and we predict some BH-NS mergers with comparable mass compact objects. This is important in context of mass ejection in BH-NS mergers (see Sec. 6).

In Figures 2 and 3 we also clearly see the effect of natal kicks on the merger rate density of BH-NS systems. For models with decreased natal kicks (e.g., M230 and M280) the rates are higher by about an order of magnitude than for models with high natal kicks (e.g., M233 and M283). This is a consequence of BH-NS progenitor binaries being disrupted more easily in models in which we employed higher natal kicks. One can also see some noisy features that appear at high mass ends. Those are the results of low statistics.

In Table 3 we list fractions of BH-NS mergers that have both compact objects within the FMG (FMGboth), only a BH in the gap (FMG_{BH}) , only an NS in the gap (FMG_{NS}) , or no components in the gap (FMG_{none}). This table contains BH-NS mergers that take place for redshifts with z < 1 and the fractions are calculated using merger rate densities (see eq. 10). For models that the employ rapid supernova engine, there are no BH-NS mergers with objects in the FMG (assumed $2.1 - 5 M_{\odot}$ range). For models that employ the delayed supernova engine remnant prescription, about half or a little more than half (0.576 - 0.708) of BH-NS mergers do not have any mass gap objects. With these models, those that employ high natal kicks independent of compact object mass (M283, M383, and M483) show a significant fraction of BH-NS mergers with both compact objects within the mass gap (0.197 - 0.212). Since all compact objects have an equal probability of getting a high natal kick and disrupting the progenitor binary, the mass function of these compact objects falls steeply off with mass (approximately following the initial mass function of the stars); see the black (NS) and green (BH) lines in Figure 3. That results in a significant fraction of BH-NS mergers with both compact objects within the FMG. In contrast, for our model in which natal kicks decrease with compact object

mass (M280), this fraction is very small (0.036) because many BH-NS systems with heavy ($\sim 10~M_{\odot}$) BHs outside the FMG are not disrupted by the kick; see the blue line in Figure 3. Depending on the model, significant fractions of BH-NS mergers (0.211 – 0.256) have one compact object (whether it is an NS or a BH) within the FMG. Although we differentiate between NSs and BHs in the mass gap in Table 3, we note that this division is arbitrary as we simply assume that any compact object above 2.5 M_{\odot} is a BH.

In Table 4 we list fractions of BH-NS mergers with compact objects within the FMG, but only for systems that are detectable by LIGO/Virgo (S/R>8; see eq. 13). The detectable LIGO/Virgo population is predicted to have a significant fraction of mergers (0.199 - 0.334) with at least one compact object within the mass gap for delayed supernova engine models (M280, M283, M383, and M483). A small but noticeable fraction (0.025 - 0.186) of BH-NS mergers are found to have both compact objects within the gap. Compared with the intrinsic population (see Table 3), the LIGO/Virgo detectable population has a smaller fraction of BHs and a larger fraction of NSs in the gap. This simply reflects the fact that LIGO/Virgo can detect heavier objects from larger distances and that light BHs within the gap tend to be less represented in the LIGO/Virgo detectable population, while NSs need to be heavy to be within the gap. Thus, NSs stand out more in this population.

The fraction of FMG+FMG mergers among the entire LIGO/Virgo detectable BH-NS merger population is significantly smaller for the low BH natal kick model (M280: ~0.04) than for high kick models (M283, M383, and M483: ~0.2; see Table 4). FMG+FMG systems tend to survive high natal kicks more often than other BH-NS merger progenitors because of their specific evolutionary history that typically leads to small separations before supernova explosions (see Sec. 4.3). Therefore, models with high natal kicks contain higher fractions of FMG+FMG systems, which are mergers that are typically accompanied by mass ejection, (see Sec. 5) and thus show kilonova emission (see Sec. 6). However, these models have small BH-NS merger rates (see Sec. 7).

We find that BH-NS mergers may still be detectable at distances as far as $z \sim 0.1$ with LIGO/Virgo during O3 (S/R > 8). Due to GW selection effects, the most distant mergers would be the most massive ones, for example: $2.2~M_{\odot}$ NS + $30.8~M_{\odot}$ BH.

Table 3. Intrinsic fraction of (z < 1) BH-NS mergers η_1 in which both (FMG_{both}) components, only a BH (FMG_{BH}) component, only an NS (FMG_{NS}) component, or no (FMG_{none}) components are within the FMG.

Model	FMG _{both}	FMG_{BH}	FMG_{NS}	FMG_{none}
M230	0	0	0	1
M233	0	0	0	1
M280	0.036	0.019	0.237	0.708
M283	0.197	0.110	0.101	0.592
M383	0.200	0.098	0.119	0.582
M483	0.212	0.107	0.104	0.576

Note: see eq. 10. The same results expressed in terms of merger rates can be found in the appendix; see Table A.1.

4. Mass ratio of BH-NS systems

In Figure 4 we show the mass ratio distribution (mass of an NS to a BH: $q = M_{NS}/M_{BH}$) for models with a rapid supernova engine (M230 and M233) and models with delayed supernova engine

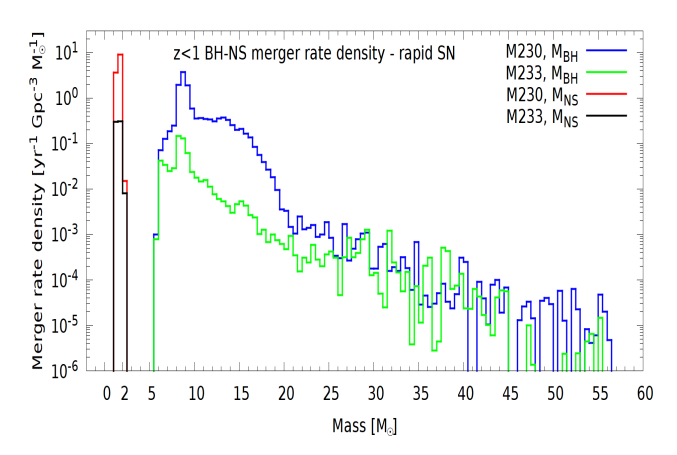


Fig. 2. Mass distribution of compact objects in BH-NS mergers in the low-redshift Universe (z < 1) for models that employ a rapid supernova engine (M230, M233). There is a very clear mass gap between NSs and BHs. It should be noted that our data become noisy for masses above $\geq 20~{\rm M}_{\odot}$. However, apparent decline in merger rate density for these higher masses is real and expected in our models.

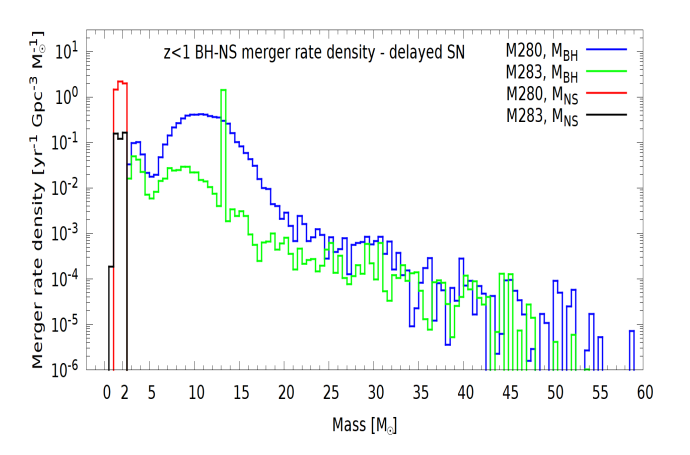


Fig. 3. Mass distribution of compact objects in BH-NS mergers in the low-redshift Universe (z < 1) for models that employ a delayed supernova engine (M280, M283). There is no mass gap between NSs and BHs. It should be noted that our data become noisy for masses above $\geq 20~{\rm M}_{\odot}$, although apparent decline in merger rate density for these higher masses is real and expected in our models.

(M280 and M283). This figure includes the population of BH-NS mergers at redshifts z < 1 and shows the intrinsic mass ratio expressed by the merger rate density in bins of $\Delta q = 0.01$.

As seen immediately from Figure 4, the majority of BH-NS mergers have small mass ratios $q \sim 0.1-0.2$ independent of model assumptions. This comes from the fact that NSs have typical masses of $1-2~{\rm M}_{\odot}$ and the majority of BHs found in BH-NS mergers in our models have a typical mass of $\sim 10~{\rm M}_{\odot}$ (see Figs. 2 and 3). Since the rapid supernova engine does not populate the mass gap, when adopting this model, we thus predict no mergers with a mass ratio larger than $q \sim 0.4$. However, for models with a delayed supernova engine, the mass ratio distribution shows a secondary peak for $q \sim 0.5-0.8$. These are BH-NS mergers with both compact objects within the FMG, as such systems must have $q \gtrsim 0.4$.

In Figure 5 we show cumulative mass ratio distribution for LIGO/Virgo detectable (S/R > 8) BH-NS mergers. In Table 5 we list fractions of LIGO/Virgo detectable BH-NS mergers

Table 4. Fraction of LIGO/Virgo (S/R > 8) BH-NS systems η_3 where both (FMG_{both}) components, only a BH (FMG_{BH}) component, only an NS (FMG_{NS}) component, or no (FMG_{none}) components are within the FMG

Model	FMG _{both}	FMG_{BH}	FMG _{NS}	FMG _{none}
M230	0	0	0	1
M233	0	0	0	1
M280	0.025	0.002	0.332	0.641
M283	0.186	0.011	0.188	0.614
M383	0.171	0.024	0.226	0.578
M483	0.159	0.010	0.193	0.638

Note: see eq. 13.

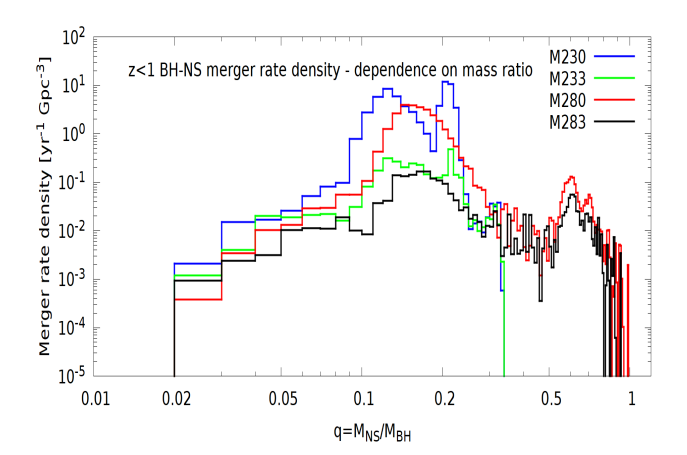


Fig. 4. Mass ratio distribution for BH-NS mergers in the low-redshift Universe (z < 1). For each BH - NS system, we calculated the mass ratio $q = M_{NS}/M_{BH} \in [0,1]$. Values indicate merger rate densities estimated from the systems within each q bin, that is to say $dRate dt^{-1}dV^{-1}dq^{-1}\Delta q$, with $\Delta q = 0.01$. For transparency purposes, we use simple merger rate density as the vertical axis label. Most mergers have rather small mass ratios $q \sim 0.1 - 0.2$, but there are also extreme mass ratio systems such as $56 \text{ M}_{\odot} \text{ BH} + 1.3 \text{ M}_{\odot} \text{ NS} (q = 0.023)$. For models with the delayed supernova engine (M280 and M283), there is a secondary peak for high mass ratios q > 0.4, which consists mostly of double compact objects with both components in the FMG (see Sec. 4).

(S/R > 8) that have a mass ratio smaller than 1/50, 1/30, 1/20, and 1/10 for all our models. Additional models that include BH-NS mergers with input physics assumptions that are different to those used in this study may be found at ² under the tab "Download/2020: Double Compact Objects/Belczynski et al. 2020".

Our results show that it is possible to create extreme mass ratio systems q < 0.05. For example, the most extreme systems detectable by LIGO/Virgo (S/R > 8) in our models are: M230 q = 0.021 ($M_{BH} = 55.0 \, \mathrm{M_\odot}$, $M_{NS} = 1.2 \, \mathrm{M_\odot}$), M233 q = 0.023 ($M_{BH} = 49.0 \, \mathrm{M_\odot}$, $M_{NS} = 1.1 \, \mathrm{M_\odot}$), M280 q = 0.025 ($M_{BH} = 52.5 \, \mathrm{M_\odot}$, $M_{NS} = 1.3 \, \mathrm{M_\odot}$), M283 q = 0.029 ($M_{BH} = 29.9 \, \mathrm{M_\odot}$, $M_{NS} = 0.9 \, \mathrm{M_\odot}$), M383 q = 0.022 ($M_{BH} = 59.5 \, \mathrm{M_\odot}$, $M_{NS} = 1.3 \, \mathrm{M_\odot}$), and M483 q = 0.021 ($M_{BH} = 60.1 \, \mathrm{M_\odot}$, $M_{NS} = 1.3 \, \mathrm{M_\odot}$).

In the next subsection we discuss in detail the formation of one extreme mass ratio system (38.9 M_{\odot} + 1.3 M_{\odot} ; Sec. 4.1), as infrequent as it may be. We follow with a detailed description of the formation of a BH-NS merger with a typical mass ratio (14.7 M_{\odot} + 1.8 M_{\odot} ; Sec. 4.2), and finish with a description of a

BH-NS merger with comparable mass components, both within the FMG (3.5 M_{\odot} + 2.1 M_{\odot} ; Sec. 4.3).

Table 5. Fraction of LIGO/Virgo detectable (S/R > 8) BH-NS mergers with extremely small ratios and extremely small mass ratios.

Model	q<1/50	q<1/30	q<1/20	q<1/10
M230	0	0.0003	0.0017	0.0332
M233	0	0.0028	0.0319	0.1071
M280	0	$< 10^{-4}$	0.0022	0.0208
M283	0	0.0017	0.0274	0.1171
M383	0	0.0023	0.0149	0.1321
M483	0	0.0047	0.0139	0.1650

Note: The same results expressed in terms of merger rates can be found in the appendix; see Table A.2.

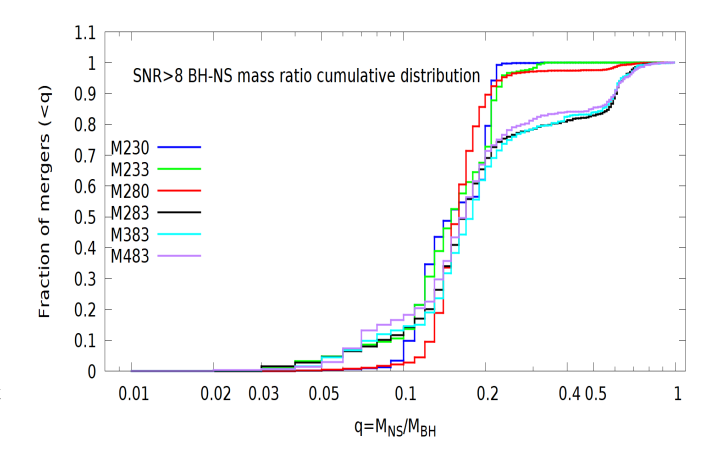


Fig. 5. Cumulative distribution of LIGO/Virgo detectable (S/R > 8) BH-NS mergers in terms of mass ratio (see also Table 5).

4.1. Extreme mass ratio BH-NS: $38.9 + 1.3 \ M_{\odot}$ merger

In this study we use the terms primary and secondary component for binary components with higher and lower zero age main sequence (ZAMS) mass, respectively. Our calculations show that BH-NS mergers (independent of their mass ratio) follow a similar evolutionary history. In Figure 6 we show the major stages of evolution of a massive binary (primary $M_1 = 91.7 \text{ M}_{\odot}$, secondary $M_2 = 9.5 \text{ M}_{\odot}$) that ultimately produces an extreme mass ratio BH-NS merger ($M_{BH} = 38.9 \text{ M}_{\odot}$, $M_{NS} = 1.3 \text{ M}_{\odot}$: q = 0.033). Below we describe the major evolutionary stages.

The evolution starts with a very massive primary ($M_A = 91.7 \, \mathrm{M}_\odot$) and an intermediate mass secondary ($M_B = 9.5 \, \mathrm{M}_\odot$) on a very wide orbit (semimajor axis $a = 7400 \, \mathrm{R}_\odot$) with a small eccentricity (e = 0.09) Next, the primary becomes a core helium burning star while the secondary is still on the main sequence. Then, a CE phase is initiated by expansion of the primary; the primary becomes a naked helium star after H-rich envelope ejection. Afterwards, the primary experiences a pair-instability pulsation supernova mass loss and immediately collapses directly to a BH. The secondary becomes a Hertzsprung Gap (HG) star and, 14 kyr later, it initiates a stable Roche lobe overflow mass transfer that ends when the secondary is in the core helium burning stage, making a blue loop on the H-R diagram (radius decreases). Then, the Roche-lobe overflow restarts while the secondary is still in the core helium burning stage and it is moving

² www.syntheticuniverse.org

redwards on the H-R diagram loop (radius increases). The Roche lobe overflow ends when the secondary loses most of its H-rich envelope. Afterwards, the secondary becomes a naked helium star and explodes in a Type Ib (core-collapse) supernova, forming an NS.

A highly eccentric BH-NS binary with an extreme mass ratio is formed. After more than 2 billion years of tightening the orbit, the merger of the BH with the NS leads to a burst of gravitational waves, but there is no mass ejection during the merger (no kilonova).

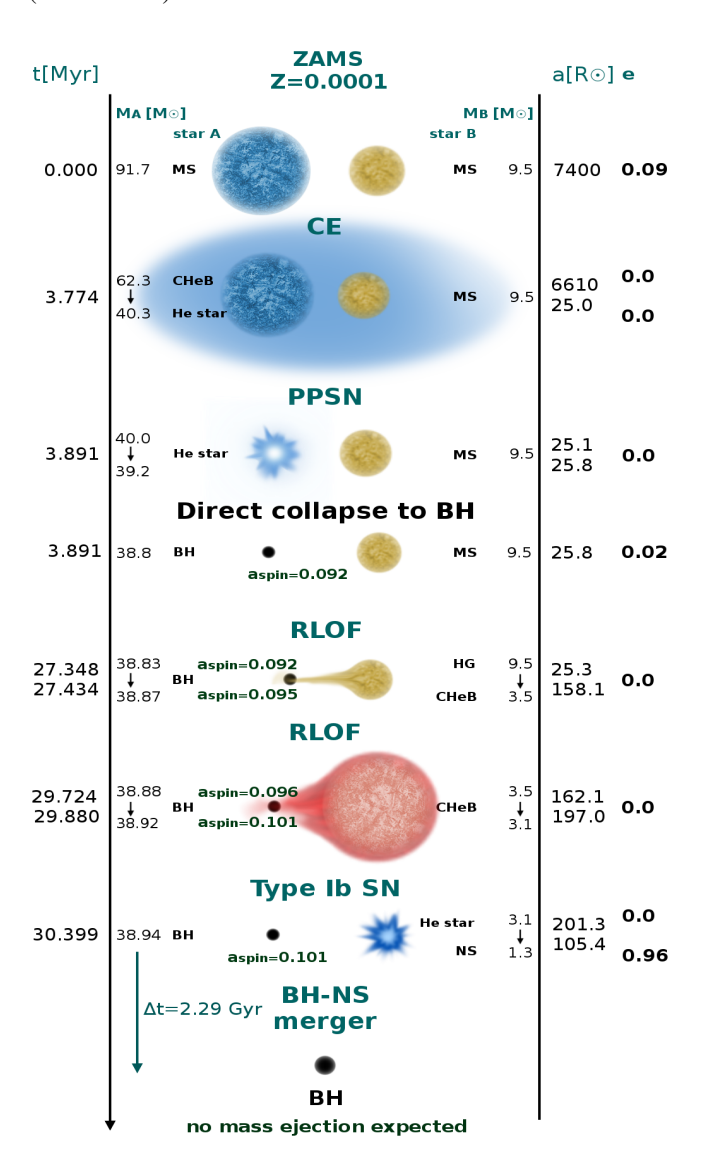


Fig. 6. Evolutionary route leading to the formation of the 38.9 $\rm M_{\odot}$ + 1.3 $\rm M_{\odot}$ (q=0.033) BH-NS merger for metallicity Z=0.0001 (model M280). The evolution from ZAMS to the formation of the BH-NS system takes ~ 30.4 Myr, and then it takes ~ 2.29 Gyr for the system to in-spiral (angular momentum loss due to the emission of gravitational waves), leading to the final merger of the two compact objects. (CHeB: core helium burning star, He star: naked helium star, HG: Hertzsprung gap star). No tidal spin-up is expected due to large orbital separations when binary components are naked helium stars: $a\sim 25~\rm R_{\odot}$ ($P_{\rm orb}=2.1\rm d$; star A) and $a\sim 200~\rm R_{\odot}$ ($P_{\rm orb}=60\rm d$; star B) (see Sec. 2.1).

There is nothing specifically unusual in the formation of extreme mass ratio BH-NS mergers. Similar evolutionary routes are responsible for nonextreme BH-NS mass ratio systems (see Klencki et al. (2018)). BH-NS progenitors experience two major binary interactions (CE and RLOF) and are subject to one strong supernova explosion forming an NS. The natal kick (243 km s⁻¹ in the case of the example shown in Fig. 6) produced during the supernova can make the BH-NS system highly eccentric. This reduces the time to final merger, allowing such systems to merge within Hubble time and to be detected by LIGO/Virgo. However, for extreme mass ratio systems there is no mass ejection during the merger and therefore these mergers are not expected to produce EM (e.g., kilonova or short GRB) signals (see Sec. 6).

4.2. Typical mass ratio BH-NS: $14.7 + 1.8 M_{\odot}$ merger

There are several variations to the formation of BH-NS mergers in respect to the evolution presented in Figure 6. Here we pick one such variation to show the formation of a typical mass ratio (q = 0.12) BH-NS merger in our simulations.

The formation of a $14.7 + 1.8 \text{ M}_{\odot}$ BH-NS merger at metallicity Z = 0.0005 (model M230) involves the evolutionary stages, which we describe below.

The evolution starts with a massive primary ($M_A = 35.8 \text{ M}_{\odot}$) and an intermediate mass secondary ($M_{\rm B} = 20.6~{\rm M}_{\odot}$) on a wide $(a = 6641 \,\mathrm{R}_{\odot})$ and eccentric orbit (e = 0.56). At some point, the primary becomes an asymptotic giant branch (AGB) star, while the secondary is still on the main sequence. As a result, the CE phase is initiated by the primary, which loses about half of its mass. Then, the primary undergoes a direct collapse (only a $0.15~M_{\odot}$ mass loss in neutrinos, no supernova explosion) to a BH and we assume no natal kick. Next, the secondary becomes a core helium burning star, initiates a second CE episode and becomes a naked helium star. Later the secondary explodes in a Type Ib/c (core-collapse) supernova, forming an NS with a high natal kick (229 km s⁻¹). Subsequently, an eccentric (e = 0.90) BH-NS binary with a moderate mass ratio forms after 10.5 Myr of evolution since ZAMS. After 2.7 Gyr, the merger of the BH with the NS leads to a burst of gravitational waves but without mass ejection or kilonova.

This typical q=0.12 system was formed from a ZAMS binary with comparable mass components: $q_{ZAMS}=0.58$, and it evolved through two CE phases. Both components evolve along similar tracks. They form remnants shortly after the CE they initiated. No tidal spin-up before the BH formation is expected: $a=557~\rm R_{\odot}$ and $P_{\rm orb}=257\rm d$. Both stars lose a significant fraction ($\gtrsim 50\%$) of their mass in CE events, and the secondary component ejects some extra mass from the binary during a Type Ib/c supernova that forms a heavy NS. A high natal kick at the NS formation leads to the formation of a very eccentric (e=0.9) BH-NS binary that can merge within the Hubble time, despite its rather large separation ($a \sim 40~\rm R_{\odot}$).

4.3. Comparable mass BH-NS: $3.5 + 2.1~M_{\odot}$ merger

Comparable mass BH-NS systems, by construction, have a highmass NS and a low-mass BH, and typically one or both of the components have mass within the FMG. Therefore, such systems appear only within delayed supernova models. Below, we present the BH-NS merger with both components within the FMG (3.5 $\rm M_{\odot}$ BH +2.1 $\rm M_{\odot}$ NS; q=0.6) that has formed at metallicity Z=0.0015 in model M280. Firstly, the ZAMS binary is formed with almost equal-mass components: 18.80 $\rm M_{\odot}$ and 18.66 $\rm M_{\odot}$ at a moderately wide ($a=1100~\rm R_{\odot}$) and eccentric (e=0.36) orbit. Later, when both components become core helium burning stars at a similar time, stable RLOF starts from the

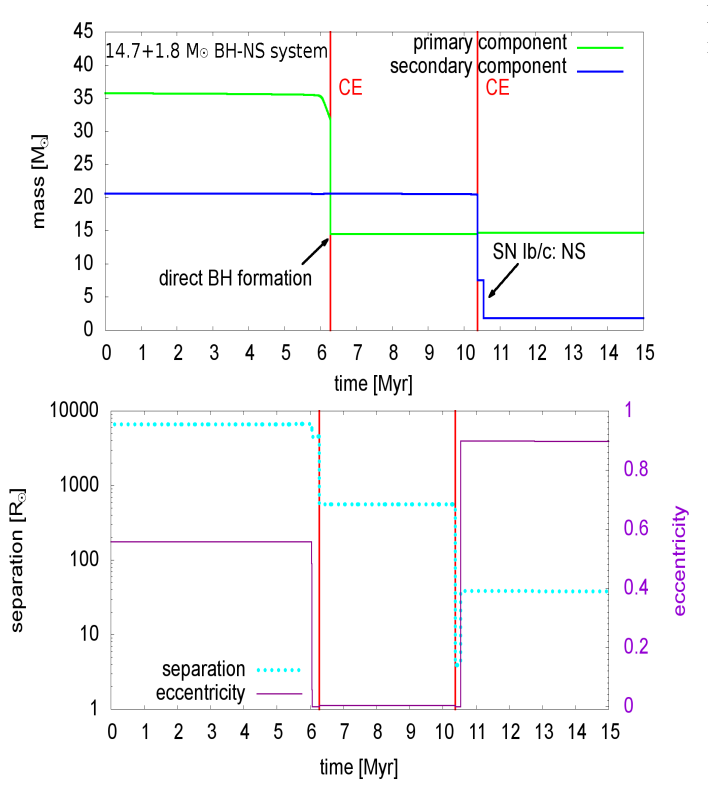


Fig. 7. Evolution of two massive stars that leads to the formation of the moderate mass ratio (q=0.12) BH-NS ($14.7+1.8~M_{\odot}$) merger (model M230). The top panel shows the mass evolution of the primary and secondary stars, while the bottom panel shows the changes in the semimajor axis and eccentricity. Evolution from ZAMS to the BH-NS system formation takes 10.5 Myr, and then it takes another 2.7 Gyr for the two compact objects to merge and produce gravitational wave radiation that is potentially detectable by LIGO/Virgo. No mass ejection (no kilonova or short GRB) is expected in this case.

primary to the secondary. As a result, the primary component becomes a naked helium star after losing its H-rich envelope. Then, the CE is initiated by the secondary component, which is still a core helium burning star. After the CE, both components are naked helium stars. However, this state is not permanent: another stable RLOF takes place from the primary (evolved naked helium star) to the secondary component (~ 2.0 M_{\odot} mass loss). As a result the primary component explodes as a stripped supernova (~ 2.6 M_{\odot} mass loss) with a 228 km s $^{-1}$ natal kick forming an NS, and the binary becomes eccentric (e=0.24). The secondary component supernova explosion forms a BH and a 217 km s $^{-1}$ natal kick reduces system eccentricity (e=0.06). Then, a close ($a=3.6~R_{\odot}$) BH-NS binary forms on an almost circular orbit after $\sim 12~Myr$ evolution since ZAMS. After another 0.6 Gyr, the BH-NS merger occurs.

In this case, the NS forms ~ 0.2 Myr before the BH forms from the primary star due to early mass ratio reversal between the primary and the secondary (first stable RLOF). Figure 8 shows the evolution of the binary progenitor of this system in more detail. The small orbital separation prior to the BH formation ($a = 2.3 \, \text{R}_{\odot}$, $P_{\text{orb}} = 0.11 \, \text{d}$) causes the WR star progenitor of the BH to be spun up due to tidal interactions. The BH spin becomes very large: $a_{spin} = 0.983$ in comparison to $a_{spin} = 0.092$ expected from single stellar evolution without tidal interactions.

Due to the high NS mass and its compactness, no mass ejection is expected even for the high spin and low mass of a BH.

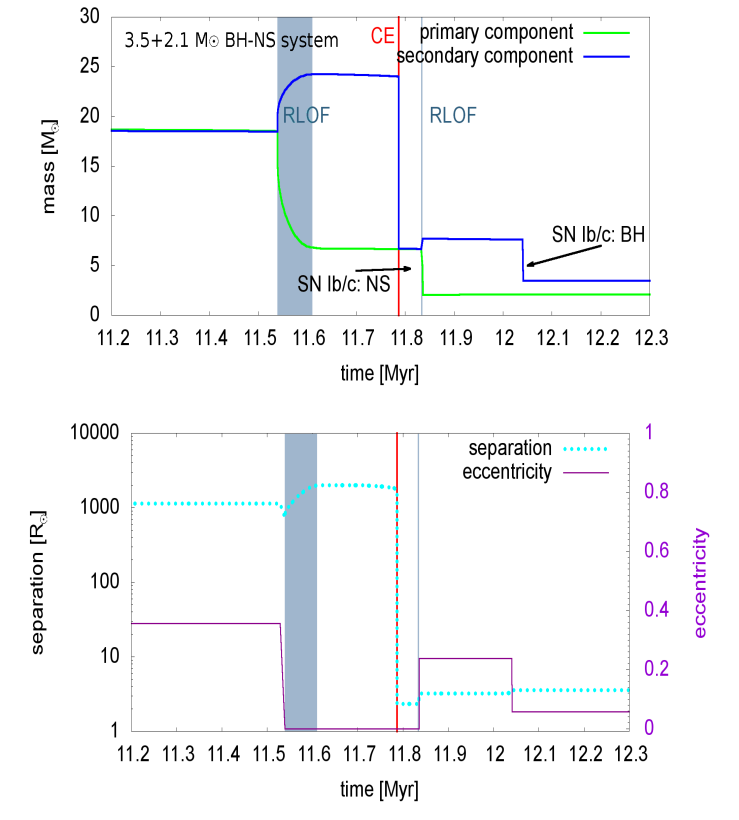


Fig. 8. Evolution of binary system that forms a $3.5 + 2.1\,$ M $_{\odot}$ BH-NS merger (mass ratio of q=0.6). We note that both compact objects are within the FMG and we expect that this merger will not lead to any mass ejection due to a high NS mass.

5. Mass ejection in BH-NS mergers

Some BH-NS mergers may produce an electromagnetic counterpart. For this to take place, the NS must disrupt outside the BH event horizon. In this section we discuss the amount of mass (if any) that is ejected during the BH-NS merger process.

Table 6. Intrinsic fraction of BH-NS mergers (z < 1) η_2 with any mass ejecta ($M_{\rm ej} > 0.001~{\rm M}_{\odot}$) and with significant mass ejecta ($M_{\rm ej} > 0.01~{\rm M}_{\odot}$).

Model	$M_{\rm ej} > 0.001 {\rm M}_{\odot}$	$M_{\rm ej} > 0.01 {\rm M}_{\odot}$
M230	0.006	0.002
M233	0.063	0.022
M280	0.006	$< 10^{-4}$
M283	0.034	$< 10^{-4}$
M383	0.087	0.038
M483	0.030	0.004

Note: see eq. 11

Table 6 shows the fraction of BH-NS mergers in our intrinsic population (z < 1; eq. 11) with any mass ejecta ($M_{\rm ej} > 0.001~{\rm M}_{\odot}$) and with significant mass ejecta ($M_{\rm ej} > 0.01~{\rm M}_{\odot}$) for all our models. The corresponding distribution and reverse cu-

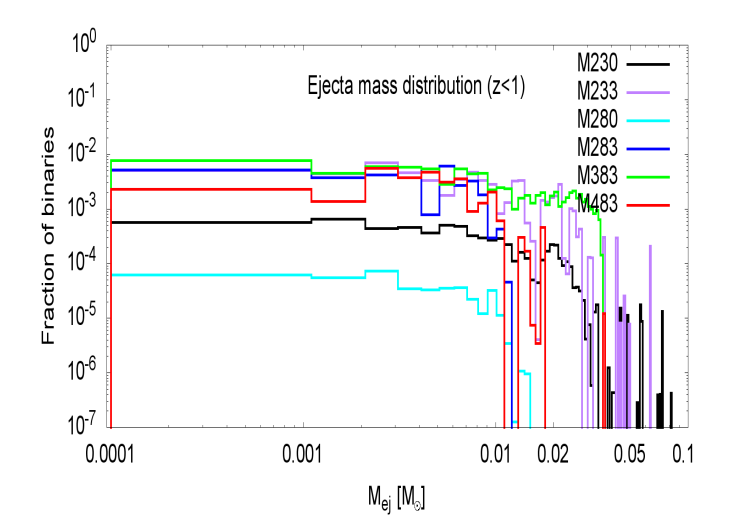


Fig. 9. Intrinsic distribution of ejecta mass in BH-NS mergers with z < 1. The structures at $M_{ej} \gtrsim 0.03 \text{ M}_{\odot}$ are shot noise.

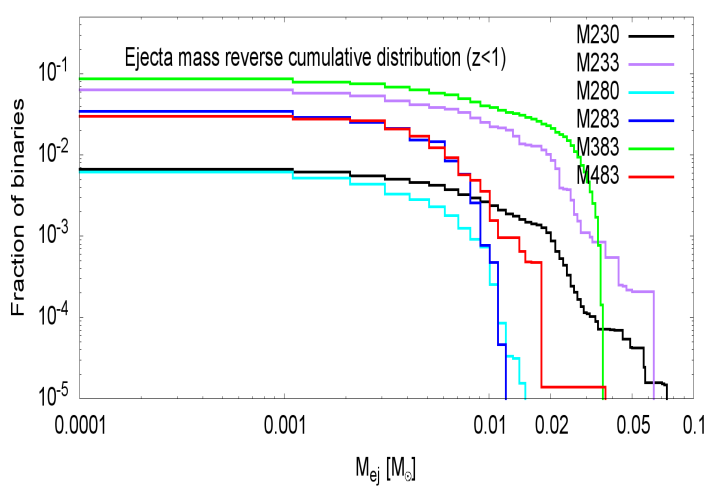


Fig. 10. Intrinsic reverse cumulative distribution of ejecta mass (> $M_{\rm ej}$) in BH-NS mergers with z < 1.

mulative³ distributions are shown in Figures 9 and 10, respectively.

The lowest ejecta mass found for BH-NS mergers produced by our simulations and calculated with equation 3 is $M_{\rm ej} = 0.0002~{\rm M}_{\odot}$, but we use $M_{\rm ej} = 0.001~{\rm M}_{\odot}$ as the threshold for marking systems with *any* mass ejection. For our models that eject mass, the number of systems with $M_{\rm ej} < 0.001~{\rm M}_{\odot}$ is negligible. The largest ejecta mass is $M_{\rm ej} \sim 0.07~{\rm M}_{\odot}$, which is consistent with the results from Rosswog (2005); Kyutoku et al. (2015); Barbieri et al. (2020). The ejecta mass estimated for the first confirmed NS-NS merger, GW170817: $\sim 0.0002 - 0.03~{\rm M}_{\odot}$ (Côté et al. 2017; Abbott et al. 2017) is in the range of our estimates.

For high BH spins (model M383; Geneva inefficient angular momentum transport), we obtain the maximum fraction of BH-NS mergers with any ejecta among our models: $\eta_2 = 0.087$ (see eq. 11). This result is more pessimistic than earlier popu-

lation synthesis predictions that showed the fraction of BH-NS mergers for rapidly spinning BHs with mass ejecta is as high as 0.4 (Belczynski et al. 2008b). This difference comes from the updated numerical simulations of ejecta mass, better constraints on the EoS, and an improved understanding of input stellar and binary physics. However, it should be noted that for low BH spins, our results are consistent with previous predictions that showed a 0.01 fraction of BH-NS mergers with mass ejecta (Belczynski et al. 2008b) . For comparison, our reference model with low BH spins (model M280: efficient MESA angular momentum transport) shows that the fraction of BH-NS mergers with any mass ejecta is comparable: $\eta_2 = 0.006$ (see Table 6).

The rapid supernova engine models (M230 and M233) produce BH-NS mergers with low-mass NSs ($\lesssim 2~M_{\odot}$) and show the larger fraction of systems with mass ejecta than the corresponding delayed supernova engine models (M280 and M283). In the delayed models, we also allow for the formation of heavy NSs ($> 2~M_{\odot}$), which are more compact than lower-mass NSs (see Fig. 1) and thus are harder to disrupt.

BH spin plays a significant role in setting the size of the event horizon and this regulates whether NS disruption can produce any mass ejecta (Foucart et al. 2018; Zappa et al. 2019; Sedda 2020). For rapidly rotating BHs (small event horizons), mass ejection is found in a small fraction of BH-NS mergers (M383) and the fraction decreases for slowly spinning BHs (M230, M233, M280, and M283). There are still some BH-NS mergers that generate mass ejection for the (almost) nonspinning BH model (M483).

Table 7 shows only those BH-NS mergers with any mass ejecta ($M_{ej} > 0.001 \, \mathrm{M}_{\odot}$; see Table 6) and we subdivide these to show the contribution of mergers in which none, one (BH or NS), or both components are within the FMG. These are, therefore, intrinsic fractions for the sub-population of BH-NS mergers (with any mass ejection) within z < 1. Models with a rapid supernova engine (M230 and M233) have both merger components always outside the FMG. However, for our reference model (M280) and two other models with a delayed supernova engine (M283 and M483) the fraction of BH-NS mergers with mass ejecta having both components in the FMG is very high (~ 0.9).

Because binaries with both objects in the FMG correspond to more favorable mass ratios for tidal disruption outside the BH horizon, the fraction of binaries in the FMG that produce mass ejecta is high for delayed supernova engine models.

In the most extreme case of our reference model (M280), we find that the fraction of BH-NS mergers with any mass ejecta that have both components within the FMG is 0.959. These BH-NS systems have evolved through spin-up of a WR star and BHs have a very large spin that allows for easy mass ejection $(a_{\rm spin} > 0.9)$. The lowest mass BHs (i.e., in the FMG) are naturally selected for systems with mass ejecta as they have the smallest event horizon. The heaviest NSs (i.e., in the FMG) are also favored since in order to spin up the BH progenitor (a WR star), either an NS forms first (so it must be heavy; mass ratio reversal), or the NS progenitor is a WR star at the time when the BH progenitor is a WR star (so both stars evolve at almost similar timescales and must be similar in mass). Additionally, this model allows for fallback-moderated natal kicks, so heavy NSs receive smaller kicks and they have an increased chance of surviving in a binary after a supernova explosion than the lighter

For the model with high initial BH spins (M383), the fraction of mergers with mass ejecta and both compact objects in the FMG is smaller (0.365), as specific processes (i.e., tidal spin up) are not the only way to produce mass ejecta.

³ By reverse cumulative distribution we mean the fraction of systems with a higher value than the current argument

Table 7. Intrinsic BH-NS merger population with any mass ejecta $(M_{ej} > 0.001 \text{ M}_{\odot}, z < 1)$.

Model	FMG _{both}	FMG _{BH}	FMG _{NS}	FMG _{none}
M230	0	0	0	1
M233	0	0	0	1
M280	0.959	0	0.005	0
M283	0.854	0.007	0.139	0
M383	0.365	0.004	0.016	0.614
M483	0.940	0	0.030	0.030

Note: see Table 6. We present the fraction of mergers for which both (FMG_{both}) components, only a BH (FMG_{BH}) component, only an NS (FMG_{NS}) component,

or no (FMG_{none}) components are within the FMG.

Table 8. LIGO/Virgo detectable BH-NS mergers (S/R > 8) with any mass ejecta $M_{ej} > 0.001 \, \mathrm{M}_{\odot}$. We present the fraction of mergers for which both (FMG_{both}) components, only a BH (FMG_{BH}) component, only an NS (FMG_{NS}) component, or no (FMG_{none}) components are within the FMG.

Model	FMG _{both}	FMG_{BH}	FMG _{NS}	FMG _{none}
M230	0	0	0	1
M233	0	0	0	1
M280	1	0	0	0
M283	0.996	0.004	0	0
M383	0.431	0.075	0	0.494
M483	0.967	0	$< 10^{-3}$	0.032

Note: we present the fraction of mergers for which both (FMG_{both}) components, only a BH (FMG_{BH}) component, only an NS (FMG_{NS}) component,

or no (FMG_{none}) components are within the FMG.

In Table 8 we list fractions of BH-NS mergers with compact objects in and out of the FMG, but only for systems that have any mass ejection ($M_{ej} > 0.001 \,\mathrm{M}_{\odot}$) and are detectable by LIGO/Virgo (S/R>8; see eq. 12). These fractions are calculated using merger rates (see eq. 14). This table shows how likely it is for a BH and an NS to be within the FMG for a LIGO/Virgo BH-NS merger that may have detectable kilonova (see Sec. 6).

The results are qualitatively similar to those we found for the intrinsic population of BH-NS mergers presented above in Table 7. The small to moderate quantitative differences arise from the fact that our adopted criteria for the LIGO/Virgo detectability set the horizon redshift for (light) BH-NS mergers with mass ejection to only $z_{\text{hor}} \sim 0.07$ (Table 8). For comparison, the horizon redshift for the overall BH-NS merger LIGO/Virgo detectable population is $z_{\text{hor}} \sim 0.1$. In contrast, the redshift cut that we employed in Table 7 is z = 1.

6. Electromagnetic counterpart

BH-NS mergers in which the NS is disrupted outside the BH event horizon produce mass ejecta and accretion disks that may produce EM counterparts. In this section we discuss our results on kilonova emission associated with BH-NS mergers with mass ejection. For LIGO/Virgo detectable events (S/R > 8), we calculate kilonova luminosities for each BH-NS merger with some mass ejecta ($M_{\rm ej} > 0.001~{\rm M}_{\odot}$) following the scheme outlined in Section 2.2. For each merger event we employ the merger distance from our synthetic Universe (see Sec. 2.3).

Figure 11 shows the distribution of brightness in o-band (1260 - 1360nm) of BH-NS mergers with kilonova emission for all our models. The distribution of kilonova brightness has = a very large range ($M_{\rm kn} \sim 15-28$ mag), but dim kilonovae dominate ($M_{\rm kn} \sim 24$ mag). Since such events can be detected only at small redshifts (see Sec. 5), we do not take into account k-correction. The large brightness range comes from the combination of distance range for BH-NS mergers that are detectable by LIGO/Virgo during O3 ($z \leq 0.07$; luminosity distance: ≤ 320Mpc) and the fact that ejecta mass is found in a wide range of values $(M_{\rm ej} \sim 0.0002 - 0.07 \, \rm M_{\odot})$. We find that most kilonovae are dim because most events are found at distances (average redshift: $z_{ave} \sim 0.04$; average luminosity distance of ~ 180Mpc) close to the LIGO/Virgo O3 detection horizon for BH-NS mergers ($z \sim 0.07$; where most of the searched volume is located). Additionally, the ejecta mass found in our simulations is rather small; typically $M_{\rm ei}$ < 0.03 M_{\odot} (see Fig. 9).

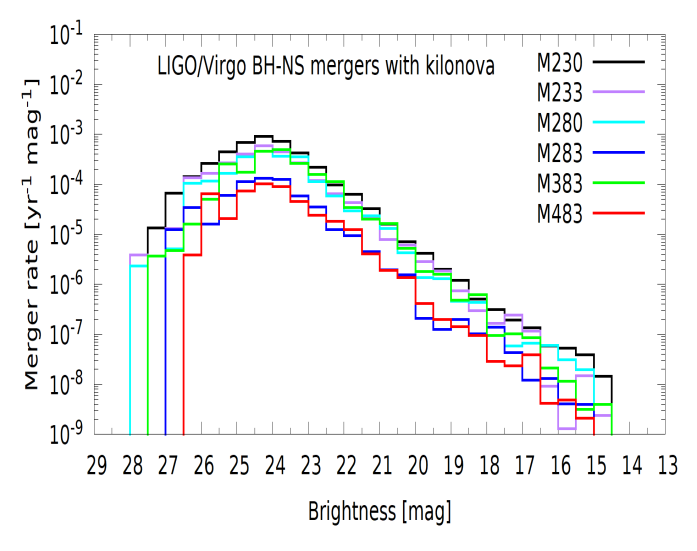


Fig. 11. Kilonova brightness distribution for LIGO/Virgo detectable (S/R > 8) BH-NS mergers.

Table 9. Fraction of BH-NS mergers with detectable kilonova among LIGO/Virgo detectable (S/R > 8) events for assumed exposure times. Kilonova detectability is assessed for three different instruments: Subaru, the Canada-France-Hawaii Telescope (CFHT) and ATLAS. The same results expressed in terms of merger rates can be found in the appendix; see Table A.3.

Model	Subaru	CFHT	ATLAS
M230	0.004	0.002	$< 10^{-5}$
M233	0.067	0.032	$< 10^{-4}$
M280	0.004	0.002	$< 10^{-5}$
M283	0.021	0.010	$< 10^{-4}$
M383	0.064	0.038	$< 10^{-4}$
M483	0.018	0.009	< 10 ⁻⁴

Note: see eq. 16.

Kilonova brightness varies with different model assumptions. In Table 9, for all our models, we show the fraction of BH-NS mergers with detectable kilonova among LIGO/Virgo detectable events (S/R > 8; see eq. 16). We identify each simulated kilonova as detectable based on the detection thresholds of some typical optical instruments used in the search for kilonovae. We show results for small instruments such as ATLAS (maximum

reach of $M_{\text{max}} = 19.5 \text{mag}$), the medium-size Canada-France-Hawaii Telescope ($M_{\text{max}} = 24.1 \text{mag}$) and the large Subaru telescope ($M_{\text{max}} = 26.0 \text{mag}$).

We find that the fraction of potentially detectable kilonovae associated with BH-NS mergers is negligible for small instruments: in 10,000 LIGO/Virgo detected BH-NS mergers, only $\lesssim 1$ could be accompanied by a kilonova. For medium size instruments, the fraction of BH-NS mergers with associated detectable kilonovae varies from small ($\lesssim 4$ kilonova detections per 100 LIGO/Virgo detections) to negligible (2 in 1000). For large telescopes, a slightly larger fraction of kilonovae can be associated with LIGO/Virgo candidates: up to ~ 7 kilonovae per 100 LIGO/Virgo BH-NS detections. Much smaller fractions are possible; for example, this fraction drops to 4 kilonovae per 1000 LIGO/Virgo BH-NS detections for our reference model (M280) for an 8-meter class telescope.

7. BH-NS merger rates

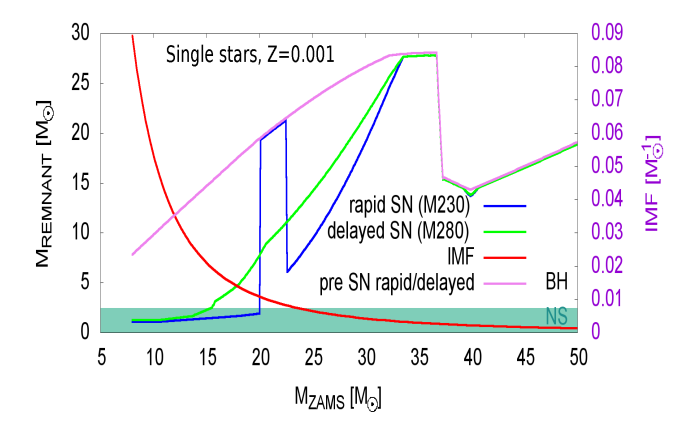
In Table 10 we list the BH-NS merger rate density $(R_{\rm d})$ obtained from our models at redshifts $z=0,\ 0.5,\ {\rm and}\ 1.$ Merger rates increase with redshift (at least until redshift z=2) correlated with an increasing star formation rate. Merger rates for models with high NS/BH natal kicks (M233, M283, M383, and M483) are lower by more than 1 order of magnitude than for models with natal kicks moderated by fallback (M230 and M280).

Comparing between models with fixed physics but different supernova engines, our merger rates are a factor of ~ 2 larger in model M230 (rapid supernova engine) compared to model M280 (delayed supernova engine). Both models employ fallback decreased natal kicks. As shown in Figure 12, BHs begin forming just above $M_{ZAMS} \sim 20 \,\mathrm{M}_{\odot}$ for the rapid supernova engine. In particular, BHs that form from the lowest mass stars ($M_{ZAMS} \sim 20 - 23 \text{ M}_{\odot}$) have large enough masses ($M_{BH} \sim$ 20 M_{\odot}) to form through direct collapse, and therefore these BHs receive no natal kicks. Binaries (potential BH-NS progenitors) with such stars always survive BH formation. On the other hand, for the delayed supernova engine, BHs begin forming just above $M_{ZAMS} \sim 15 \text{ M}_{\odot}$. In the mass range $M_{ZAMS} \sim 15 - 23 \text{ M}_{\odot}$, these BHs form with low mass ($M_{\rm BH} \lesssim 10~{\rm M}_{\odot}$) and they tend to receive high natal kicks that can easily disrupt binary progenitors of BH-NS mergers. This leads to the BH-NS merger rate difference between models that employ rapid and delayed supernova engines. There are also some differences between the models for higher initial star masses in terms of BH masses and natal kicks, but they are not that important due to the steep IMF adopted in our calculations. The emergence of a peak in BH mass in the initial-final mass relation associated with the transition between NS and BH formation ($M_{ZAMS} \sim 20 \text{ M}_{\odot}$) for the rapid supernova engine, and the continuous gradual BH mass increase with the initial star mass (at least for $M_{ZAMS} \lesssim 35 \text{ M}_{\odot}$) for the delayed supernova engine are the major reasons behind the rate difference. These particular features of BH mass dependence on initial star mass were explained in the context of underlying hydrodynamical simulations of supernova explosions that were used to create both supernova engine models (Fryer et al. 2012; Belczynski et al. 2012).

In previous sections we presented all of our results in terms of fractions of the BH-NS merger population. The rates listed in Table 10 can be used to convert these fractions to merger rate densities. In some cases, a high merger rate can compensate for a low fraction of BH-NS mergers with desired properties, or viceversa. For example, we estimated that the highest fraction of LIGO/Virgo detected BH-NS mergers will be associated with

Table 10. Intrinsic BH-NS merger rate density R_d [$Gpc^{-3} yr^{-1}$].

model	$R_{\rm d} \ (z = 0.0)$	$R_{\rm d} \ (z = 0.5)$	$R_{\rm d} \ (z = 1.0)$
M230	6.759	13.189	24.924
M233	0.328	0.647	1.196
M280	3.188	6.166	11.008
M283	0.245	0.463	0.859
M383	0.276	0.474	0.889
M483	0.214	0.412	0.732



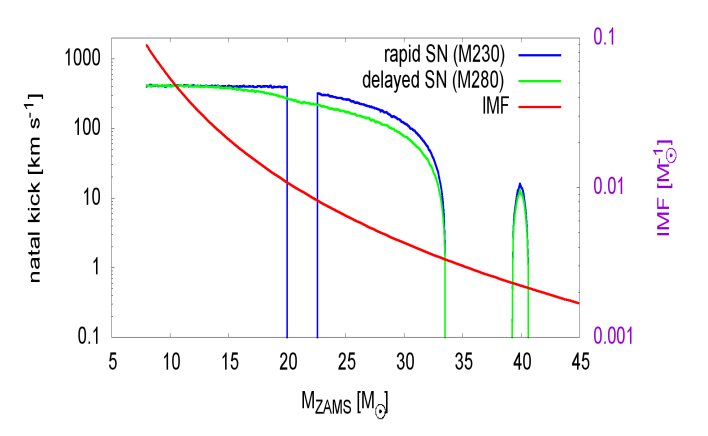


Fig. 12. Top: initial (ZAMS) star mass vs. final ($M_{remnant}$) mass relation for single stars with a metallicity of Z=0.001 for two supernova engines: rapid employed (e.g., in model M230) and delayed employed (e.g., in model M280). The blue strip at the bottom marks the NS mass range adopted in our models ($M_{\rm NS}=1-2.5~{\rm M}_{\odot}$). Bottom: fallback decreased natal kicks received by remnants (NS or BH) formed out of single stars (Z=0.001) for a given initial (ZAMS) mass for the two supernova engines. The shape of the adopted initial mass function (IMF) is also shown.

kilonovae for models M233 and M383, while other models provide $\sim 3-16$ times smaller fractions (see Table 9). However, models M233 and M383 have much smaller (by $\lesssim 10$) BH-NS merger rate densities than models M230 and M280.

The merger rate density of BH-NS systems was estimated from the O1 and O2 LIGO/Virgo observations to be $< 610 \, \mathrm{Gpc^{-3}} \, \mathrm{yr^{-1}}$ (Abbott et al. 2019b). Using one BH-NS merger candidate from the O3 LIGO/Virgo observations (GW190814), Belczynski et al. (2020) estimated the rate density of BH-NS mergers to be in the range of $1.6-60 \, \mathrm{Gpc^{-3}} \, \mathrm{yr^{-1}}$. However, it was noted by the LIGO/Virgo Collaboration that this may be a BH-BH merger (Abbott et al. 2020). More recently, based on

two BH-NS merger candidates (GW200105 and GW200115), the LIGO/Virgo Collaboration estimated the BH-NS merger rate to be in the range of $7.4 - 320 \text{ Gpc}^{-3} \text{ yr}^{-1}$ (90% credible level; The LIGO Scientific Collaboration et al. (2021)).

Our calculated BH-NS merger rate densities among the tested models are: $0.2 - 6.7 \,\text{Gpc}^{-3} \,\text{yr}^{-1}$ (z = 0), $0.4 - 13.2 \,\text{Gpc}^{-3} \,\text{yr}^{-1}$ (z = 0.5), and $0.7 - 24.9 \,\text{Gpc}^{-3} \,\text{yr}^{-1}$ (z = 1). These predicted rates are somewhat small compared to the most recent LIGO/Virgo estimates, especially since LIGO/Virgo can currently detect BH-NS mergers only to a redshift of $z \sim 0.1$. There are a number of factors that have a significant impact on merger rates and that we have not tested here. The star formation rate and associated cosmic metallicity evolution have nontrivial impacts on derived merger rates (Chruslinska et al. 2019: Chruslinska & Nelemans 2019; Tang et al. 2020; Boco et al. 2021; Santoliquido et al. 2021). New developments to understand the physics of the formation of merging double compact objects may also lead to significant changes in merger rates. For example, in this study we limited our modeling to the formation of BH-NS mergers through the CE isolated binary evolution channel. However, a non-CE channel of isolated binary evolution may produce BH-NS mergers as well, altering the merger rates and BH-NS properties (van den Heuvel et al. 2017; Stevenson et al. 2019; Neijssel et al. 2019; Shao & Li 2021; Olejak et al. 2021). We plan to dedicate a separate study to assessing the impact of these processes on BH-NS merger populations.

8. Conclusions

We performed a suite of binary evolution calculations to model a population of BH-NS mergers. Such mergers are gravitational wave sources and can potentially also produce EM emission (e.g., kilonova, short GRB). They are also interesting in the context of existence (or inexistence) of the FMG, the dearth of compact objects (whether they are NSs or BHs) in the mass range $\sim 2-5~M_{\odot}$. At present, it seems that EM observations are beginning to place some compact objects in this mass range (Cromartie et al. 2019; Thompson et al. 2019), and the same is found for GW LIGO/Virgo detections (Abbott et al. 2020). Our study may be summarized as follows:

- 1. We predict that only a very small fraction of BH-NS systems will be accompanied by mass ejection during the merger process. The fraction of such systems within the overall BH-NS merger population depends sensitively (0.6 - 9%); see Table 6) on uncertain input physics. For our best guesses of input physics (model M280), we predict that $\leq 1\%$ of BH-NS mergers are accompanied by mass ejection and by kilonovae bright enough to be detectable with a large 8-meter class telescope. This result was obtained for a specific MPA1EoS (see Fig. 1) and for rather optimistic assumptions on kilonova detectability (see Sec. 2.4). Since the mass ejection (and EM detectability) depends sensitively on BH spin, the future detections (or lack thereof) of BH-NS mergers in EM may distinguish among several existing models of angular momentum transport in massive stars that sets the BH natal spin (Bavera et al. 2020; Belczynski et al. 2020).
- 2. If more compact objects within the FMG are found, this would place limits such as those assumed in the "delayed" explosion scenario from Fryer et al. (2012), with weaker explosions with material accretion (e.g., fallback) after the launch of the explosion. A qualitatively similar result is also obtained by Zevin et al. (2020). In our scenarios with a delayed supernova engine, we find that a significant fraction of

- BH-NS mergers may host a FMG compact object: $\gtrsim 30\%$ (models M280, M283, M383, and M483; see Table 3).
- 3. Our models indicate that extreme BH-NS mass ratio systems may form in classical isolated binary evolution. For example, it is possible for systems to form with a mass ratio (NS mass to BH mass) as low as q=0.02 with $\sim 1~{\rm M}_{\odot}$ NS and $\sim 50~{\rm M}_{\odot}$ BH. However, such systems are only a very small part of the overall BH-NS merger population, and typical BH-NS mergers are expected to form with mass ratios of q=0.1-0.2.

Our current binary evolution models with BH-NS mergers (and also with BH-BH and NS-NS) mergers are publicly available for further exploration at ⁴.

9. Acknowledgements

We would like to thank the anonymous referee for their very useful and detailed comments and suggestions that helped to improve our manuscript. We would like to thank Ben Farr, Martyna Chruslinska, Coen Neijssel, Zoheyr Doctor and all the participants of the "Astrophysics of LIGO/Virgo sources in O3 era" conference who suggested research improvements. ROS would like to thank Erika Holmbeck for her helpful discussions. KB and PD acknowledge support from the Polish National Science Center (NCN) grant Maestro (2018/30/A/ST9/00050). TB was supported by the FNP grant Team/2016-3/19 and NCN grant UMO-2017/26/M/ST9/00978. ROS acknowledges support from NSF AST-1909534.

References

Abbott, B., Abbott, R., Abbott, T., et al. 2019, Physical Review X, 9, 031040 Abbott, B., Abbott, R., Abbott, T., et al. 2018a, Physical review letters, 121, 161101

Abbott, B. P., Abbott, R., Abbott, T., et al. 2018b, Living Reviews in Relativity, 21, 3

Abbott, B. P., Abbott, R., Abbott, T., et al. 2017, arXiv preprint arXiv:1710.05836

Abbott, B. P., Abbott, R., Abbott, T. D., et al. 2019a, ApJ, 882, L24

Abbott, B. P., Abbott, R., Abbott, T. D., et al. 2019b, Physical Review X, 9, 031040

Abbott, R., Abbott, T. D., Abraham, S., et al. 2021, ApJ, 915, L5

Abbott, R., Abbott, T. D., Abraham, S., et al. 2020, ApJ, 896, L44

Ade, P. A., Aghanim, N., Arnaud, M., et al. 2016, Astronomy & Astrophysics, 594, A13

Aghanim, N., Akrami, Y., Ashdown, M., et al. 2018, arXiv preprint arXiv:1807.06209

Akmal, A., Pandharipande, V., & Ravenhall, D. 1998, Physical Review C, 58, 1804

Alvarez-Castillo, D., Ayriyan, A., Benic, S., et al. 2016, The European Physical Journal A, 52, 69

Bailyn, C. D., Jain, R. K., Coppi, P., & Orosz, J. A. 1998, The Astrophysical Journal, 499, 367

Barbieri, C., Salafia, O., Colpi, M., Ghirlanda, G., & Perego, A. 2020, arXiv preprint arXiv:2002.09395

Bavera, S. S., Fragos, T., Qin, Y., et al. 2020, A&A, 635, A97

Belczynski, K., Bulik, T., & Bailyn, C. 2011, ApJ, 742, L2

Belczynski, K., Bulik, T., & Fryer, C. L. 2012, arXiv e-prints, arXiv:1208.2422 Belczynski, K., Bulik, T., Fryer, C. L., et al. 2010, The Astrophysical Journal, 714, 1217

Belczynski, K., Bulik, T., Mandel, I., et al. 2013, ApJ, 764, 96

Belczynski, K., Holz, D. E., Bulik, T., & O'Shaughnessy, R. 2016, Nature, 534, 512

Belczynski, K., Kalogera, V., & Bulik, T. 2002, The Astrophysical Journal, 572, 407

Belczynski, K., Kalogera, V., Rasio, F. A., et al. 2008a, The Astrophysical Journal Supplement Series, 174, 223

Belczynski, K., Klencki, J., Fields, C. E., et al. 2020, A&A, 636, A104

⁴ https://syntheticuniverse.org

- Belczynski, K., Repetto, S., Holz, D. E., et al. 2016, The Astrophysical Journal, 819, 108
- Belczynski, K., Taam, R. E., Kalogera, V., Rasio, F. A., & Bulik, T. 2007, The Astrophysical Journal, 662, 504
- Belczynski, K., Taam, R. E., Rantsiou, E., & Van Der Sluys, M. 2008b, The Astrophysical Journal, 682, 474
- Belczynski, K., Wiktorowicz, G., Fryer, C. L., Holz, D. E., & Kalogera, V. 2012, The Astrophysical Journal, 757, 91
- Beldycki, B. & Belczynski, K. 2016, Acta Astron., 66, 347
- Bhattacharya, M., Kumar, P., & Smoot, G. 2019, Monthly Notices of the Royal Astronomical Society, 486, 5289
- Boco, L., Lapi, A., Chruslinska, M., et al. 2021, ApJ, 907, 110
- Chruslinska, M. & Nelemans, G. 2019, MNRAS, 1974
- Chruslinska, M., Nelemans, G., & Belczynski, K. 2019, MNRAS, 482, 5012
- Côté, B., Belczynski, K., Fryer, C. L., et al. 2017, ApJ, 836, 230
- Cromartie, H., Fonseca, E., Ransom, S. M., et al. 2019, arXiv preprint arXiv:1904.06759
- de Mink, S. E. & Belczynski, K. 2015, ApJ, 814, 58
- Dominik, M., Belczynski, K., Fryer, C., et al. 2012, The Astrophysical Journal,
- Ekström, S., Georgy, C., Eggenberger, P., et al. 2012, Astronomy & Astrophysics, 537, A146
- Farr, W. M., Sravan, N., Cantrell, A., et al. 2011, The Astrophysical Journal, 741, 103
- Fontes, C., Fryer, C., Hungerford, A., Wollaeger, R., & Korobkin, O. 2020, Monthly Notices of the Royal Astronomical Society, 493, 4143
- Foucart, F., Hinderer, T., & Nissanke, S. 2018, Phys. Rev. D, 98, 081501
- Fragione, G. & Loeb, A. 2019, Monthly Notices of the Royal Astronomical Society, 486, 4443
- Fragione, G., Loeb, A., & Rasio, F. A. 2020, The Astrophysical Journal Letters, 895, L15
- Fryer, C. L., Belczynski, K., Wiktorowicz, G., et al. 2012, The Astrophysical Journal, 749, 91
- Fryer, C. L. & Kalogera, V. 2001, ApJ, 554, 548
- Fuller, J. & Ma, L. 2019, The Astrophysical Journal Letters, 881, L1
- Fuller, J., Piro, A. L., & Jermyn, A. S. 2019, Monthly Notices of the Royal Astronomical Society, 485, 3661
- Gao, H., Ai, S.-K., Cao, Z.-J., et al. 2020, Frontiers of Physics, 15, 1
- Gomez, S., Hosseinzadeh, G., Cowperthwaite, P. S., et al. 2019, ApJ, 884, L55 Greiner, J., Burgess, J. M., Savchenko, V., & Yu, H. F. 2016, ApJ, 827, L38
- Gupta, A., Gerosa, D., Arun, K., Berti, E., & Sathyaprakash, B. 2019, arXiv preprint arXiv:1909.05804
- Hinderer, T., Nissanke, S., Foucart, F., et al. 2019, Phys. Rev. D, 100, 063021
- Hinshaw, G., Larson, D., Komatsu, E., et al. 2013, The Astrophysical Journal Supplement Series, 208, 19
- Hobbs, G., Lorimer, D. R., Lyne, A. G., & Kramer, M. 2005, MNRAS, 360, 974 Hotokezaka, K. & Piran, T. 2017, The Astrophysical Journal, 842, 111
- Ivanova, N., Justham, S., Chen, X., et al. 2013, The Astronomy and Astrophysics Review, 21, 59
- Kawaguchi, K., Kyutoku, K., Shibata, M., & Tanaka, M. 2016, The Astrophysical Journal, 825, 52
- Klencki, J., Moe, M., Gladysz, W., et al. 2018, Astronomy & Astrophysics, 619, A77
- Korobkin, O., Wollaeger, R., Fryer, C., et al. 2020, arXiv e-prints, arXiv:2004.00102
- Kreidberg, L., Bailyn, C. D., Farr, W. M., & Kalogera, V. 2012, ApJ, 757, 36 Kroupa, P. 2001, Monthly Notices of the Royal Astronomical Society, 322, 231 Kyutoku, K., Ioka, K., Okawa, H., Shibata, M., & Taniguchi, K. 2015, Physical
- Review D, 92, 044028 Lee, W. H. & Kluzniak, W. 1995, Acta Astron., 45, 705
- Li, L.-X. & Paczyński, B. 1998, The Astrophysical Journal Letters, 507, L59
- Liu, K., Eatough, R. P., Wex, N., & Kramer, M. 2014, MNRAS, 445, 3115
- MacLeod, M., Antoni, A., Murguia-Berthier, A., Macias, P., & Ramirez-Ruiz, E. 2017, ApJ, 838, 56
- Madau, P. & Fragos, T. 2017, The Astrophysical Journal, 840, 39 Metzger, B. D. 2017, Living Reviews in Relativity, 20, 3
- Miller, J. M., Ryan, B. R., Dolence, J. C., et al. 2019a, Phys. Rev. D, 100, 023008 Miller, M. C., Lamb, F. K., Dittmann, A. J., et al. 2019b, ApJ, 887, L24
- Miyazaki, S., Komiyama, Y., Sekiguchi, M., et al. 2002, Publications of the Astronomical Society of Japan, 54, 833
- Mondal, S., Belczyński, K., Wiktorowicz, G., Lasota, J.-P., & King, A. R. 2020, MNRAS, 491, 2747
- Neijssel, C. J., Vigna-Gómez, A., Stevenson, S., et al. 2019, MNRAS, 490, 3740 Nissanke, S., Kasliwal, M., & Georgieva, A. 2013, ApJ, 767, 124
- Olejak, A., Belczynski, K., & Ivanova, N. 2021, arXiv e-prints, arXiv:2102.05649
- Özel, F., Psaltis, D., Narayan, R., & McClintock, J. E. 2010, The Astrophysical Journal, 725, 1918
- Paczyński, B. 1991, in American Institute of Physics Conference Series, Vol. 265, American Institute of Physics Conference Series, 144-148

- Pavlovskii, K., Ivanova, N., Belczynski, K., & Van, K. X. 2017, MNRAS, 465,
- Podsiadlowski, P., Joss, P., & Hsu, J. 1992, The Astrophysical Journal, 391, 246 Postnov, K., Kuranov, A., & Simkin, I. 2019, Astronomy Letters, 45, 728
- Qin, Y., Fragos, T., Meynet, G., et al. 2018, Astronomy & Astrophysics, 616, A28
- Rosswog, S. 2005, The Astrophysical Journal, 634, 1202
- Ruffert, M., Janka, H. T., Takahashi, K., & Schaefer, G. 1997, A&A, 319, 122
- Sana, H., De Mink, S., de Koter, A., et al. 2012, Science, 337, 444
- Santoliquido, F., Mapelli, M., Giacobbo, N., Bouffanais, Y., & Artale, M. C. 2021, MNRAS, 502, 4877
- Sedda, M. A. 2020, Communications Physics, 3, 1
- Shao, Y. & Li, X.-D. 2021, arXiv e-prints, arXiv:2107.03565
- Spruit, H. C. 1999, A&A, 349, 189
- Stevenson, S., Sampson, M., Powell, J., et al. 2019, arXiv e-prints [arXiv:1904.02821]
- Tang, P. N., Eldridge, J. J., Stanway, E. R., & Bray, J. C. 2020, MNRAS, 493, L6
- The LIGO Scientific Collaboration, The Virgo Collaboration, & The KAGRA Scientific Collaboration. 2021, arXiv e-prints, arXiv:2111.03634
- Thompson, T. A., Kochanek, C. S., Stanek, K. Z., et al. 2019, Science, 366, 637 van den Heuvel, E. P. J., Portegies Zwart, S. F., & de Mink, S. E. 2017, MNRAS, 471, 4256
- Vink, J. S., de Koter, A., & Lamers, H. 2001, Astronomy & Astrophysics, 369, 574
- Webbink, R. 1984, The Astrophysical Journal, 277, 355
- Wiringa, R. B., Fiks, V., & Fabrocini, A. 1988, Physical Review C, 38, 1010 Wollaeger, R. T., Fryer, C. L., Fontes, C. J., et al. 2019, The Astrophysical Journal, 880, 22
- Wollaeger, R. T., Korobkin, O., Fontes, C. J., et al. 2018, Monthly Notices of the Royal Astronomical Society, 478, 3298
- Zappa, F., Bernuzzi, S., Pannarale, F., Mapelli, M., & Giacobbo, N. 2019, Physical review letters, 123, 041102
- Zevin, M., Spera, M., Berry, C. P. L., & Kalogera, V. 2020, ApJ, 899, L1
- Zhang, N.-B. & Li, B.-A. 2019, arXiv preprint arXiv:1904.10998
- Zhu, Y., Wollaeger, R. T., Vassh, N., et al. 2018, The Astrophysical Journal Letters, 863, L23

Appendix A: Merger rates

In Table A.1 we list the intrinsic merger rate density of BH-NS systems with compact objects in the FMG for all models and for the local Universe ($z \sim 0$). Data in this table are the combination of Table 3 and the first column of Table 10. In other words, it is assumed that fractions of BH-NS mergers with various combinations of compact objects in the FMG (Tab. 3) are constant in the redshift range z = 0 - 1.

In Table A.2 we list the merger rate density of LIGO/Virgo detectable BH-NS systems with extreme and small mass ratios for all the models. Data in this Table are the combination of Table 5 and the first column of Table 10 (local Universe $z \sim 0$).

In Table A.3 we list the merger rate density of LIGO/Virgo detectable BH-NS systems with detectable kilonovae for all the models. Data in this Table are the combination of Table 9 and the first column of Table 10 (local Universe $z \sim 0$).

Table A.1. Intrinsic merger rate density [Gpc^{-3} yr^{-1}] of BH-NS systems in which both (FMG_{both}) components, only a BH (FMG_{BH}) component, only an NS (FMG_{NS}) component, or no (FMG_{none}) components are within the FMG.

Model	FMG _{both}	FMG_{BH}	FMG_{NS}	FMG _{none}
M230	0.000	0.000	0.000	6.759
M233	0.000	0.000	0.000	0.328
M280	0.115	0.061	0.756	2.257
M283	0.048	0.027	0.025	0.145
M383	0.055	0.027	0.033	0.161
M483	0.045	0.023	0.022	0.123

Table A.2. Merger rate density [$Gpc^{-3}yr^{-1}$] of LIGO/Virgo detectable (S/R > 8) BH-NS systems with extreme and small mass ratios.

Model	q<1/50	q<1/30	q<1/20	q<1/10
M230	0.000	0.002	0.011	0.224
M233	0.000	0.001	0.010	0.035
M280	0.000	0.000	0.007	0.066
M283	0.000	0.004	0.007	0.029
M383	0.000	0.001	0.004	0.036
M483	0.000	0.001	0.003	0.035

Table A.3. Merger rate density [$Gpc^{-3}yr^{-1}$] of BH-NS systems with detectable kilonova among LIGO/Virgo detectable (S/R > 8) events for our assumed exposure times.

Model	Subaru	CFHT	ATLAS
M230	0.0270	0.0135	$< 10^{-5}$
M233	0.0220	0.0105	$< 10^{-4}$
M280	0.0128	0.0064	$< 10^{-5}$
M283	0.0051	0.0025	$< 10^{-3}$
M383	0.0177	0.0105	$< 10^{-4}$
M483	0.0039	0.0019	$< 10^{-4}$

The kilonova detectability is assessed for Subaru, the Canada-France-Hawaii Telescope (CFHT) and ATLAS.